Loss of Bbs8 leads to cystic kidney disease in mice and affects tubulin acetylation through HDAC2

Emilia Kieckhöfer[1,2], Peter A. Matthiessen[3], Lena K. Ebert[1,2], Christina Klausen[4], Dagmar Wachten[4], Thomas Benzing[1,2], Helen May-Simera[3,*], Bernhard Schermer[1,2,*,§]

[1] *Department II of Internal Medicine and Center for Molecular Medicine Cologne, University of Cologne, Faculty of Medicine and University Hospital Cologne, Cologne, Germany*

[2] *Cologne Excellence Cluster on Cellular Stress Responses in Aging-Associated Diseases (CECAD), University of Cologne, Faculty of Medicine and University Hospital Cologne, Cologne, Germany*

[3] *Faculty of Biology, Ciliary Cell Biology Institute of Molecular Physiology, Johannes Gutenberg-University, Mainz, Germany*

[4] *Institute of Innate Immunity, Biophysical Imaging, Medical Faculty, University of Bonn, Bonn, Germany.*

**** These authors contributed equally***

[§]***corresponding author:*** bernhard.schermer@uk-koeln.de

Keywords: BBS, primary cilium, kidney, ciliopathies, cysts, HDAC2

Abstract

Bardet-Biedl Syndrome (BBS) is a genetic disorder marked by considerable genetic and phenotypic diversity. BBS often presents as a combination of retinitis pigmentosa, obesity, polydactyly, and cystic kidney disease and is considered a model ciliopathy. The syndrome is caused by pathogenic variants in BBS genes, some of which encode components of a ciliary multi-protein complex, known as the BBSome, as well as a chaperonin-like complex, which is required for BBSome assembly. In this study, we describe the occurrence of kidney cysts in a BBS mouse model. Specifically, loss of BBS8 led to the development of cystic kidney disease by the end of the first year of life. In addition to transcriptional changes of key genes involved in regulated cell death and inflammation, proteomic approaches revealed increased expression and altered phosphorylation of histone deacetylase HDAC2 in knockout kidneys. Consistently, loss of *Bbs8* resulted in a reduction of acetylated alpha-tubulin in primary cilia. This leads to diminished stability and altered dynamics of primary cilia, potentially contributing to the formation of cystic kidneys and other BBS manifestations previously described in *Bbs8* deficient mice.

Introduction

The primary cilium is a specialized microtubule-based sensory organelle that extends from the surface of most mammalian cells (Pazour and Bloodgood, 2008). It consists of the axoneme, ensheathed by the ciliary membrane, the transition zone and the basal body, which anchors the cilium to the cell body. The transition zone, located between the basal body and the main ciliary shaft, is critical for protein trafficking to and from the ciliary compartment (Reiter, Blacque and Leroux, 2012; Garcia-Gonzalo and Reiter, 2017). Stringent regulation of the protein composition is required for cilia to function as a hub for chemo- and mechano-transduction, as well as signaling (Reiter, Blacque and Leroux, 2012) and as such, primary cilia play a pivotal role in modulating various signaling pathways, e.g. Hedgehog, Wnt, and TGF-β signaling (Fan and Tessier-Lavigne, 1994; Munsterberg *et al.*, 1995; Pourquié *et al.*, 1996). Unlike any other organelle, cilia periodically disappear during the mitotic cell cycle: When cells re-enter mitosis, cilia are typically disassembled to subsequently release the basal body, a modified mother centriole, to serve as microtubule organizing centers at the spindle poles. Disassembly of cilia mechanistically involves the deacetylation and thus destabilization of microtubules among others (Pugacheva *et al.*, 2007; Gopalakrishnan *et al.*, 2023). It is well established that pathogenetic variants in proteins, which alter the structure or function of cilia, lead to a heterogeneous group of genetic diseases and syndromes referred to as ciliopathies (Hildebrandt, Benzing and Katsanis, 2011). Ciliopathies comprise a diverse group of genetic disorders with overlapping manifestations in different organs and tissues, such as the brain, eye, skeleton, liver, vasculature and kidney (Forsythe and Beales, 2013; Reiter and Leroux, 2017). Thereby, cystic and fibrotic kidney disease is a common occurrence among many ciliopathies, leading to the frequent classification of a significant

35 subgroup, namely the renal ciliopathies (Hildebrandt and Zhou, 2007; McConnachie, Stow and Mallett,
36 2021).

37 The Bardet-Biedl-Syndrome (Bardet, 1995; Biedl, 1995; Laurence and Moon, 1995) is an archetypical
38 autosomal-recessive ciliopathy characterized by obesity, retinopathy, polydactyly and kidney disease
39 (Forsythe and Beales, 2013). This syndrome is caused by mutations in BBS genes leading to
40 pathogenetic variants of BBS proteins. BBS proteins can be classified according to the particular protein
41 complex they are part of. The so called BBSome complex (Nachury *et al.*, 2007; Loktev *et al.*, 2008)
42 (BBS1, BBS2, BBS4, BBS5, BBS7, BBS8, BBS9, BBS18) is required for trafficking of ciliary membrane
43 proteins. The 2nd group of BBS proteins build the chaperonin-like complex (BBS6, BBS10 and BBS12),
44 which catalyzes the assembly of the BBSome (Seo *et al.*, 2010). The remaining BBS proteins have
45 varying specific functions but are ultimately thought to influence ciliary trafficking.

46 Studies on various *Bbs* mutant mice, including *Bbs1*^{M390R} transgenic, *Bbs2*$^{-/-}$, *Bbs4*$^{-/-}$, *Bbs5*$^{-/-}$, *Bbs6*$^{-/-}$,
47 *Bbs8*$^{-/-}$ and *Bbs10*$^{-/-}$, revealed significant parallels to human disease. These mice exhibit a broad
48 spectrum of vision impairment, obesity, male fertility impairment, and neurological deficits (Kulaga *et*
49 *al.*, 2004; Mykytyn *et al.*, 2004; Nishimura *et al.*, 2004; Fath *et al.*, 2005; Davis *et al.*, 2007; Rahmouni
50 *et al.*, 2008; Seo *et al.*, 2009; Cognard *et al.*, 2015; Bentley-Ford *et al.*, 2021). For BBS10, total body
51 knockout resulted in renal abnormalities primarily affecting glomeruli and podocytes without any cyst
52 formation, while a tubular epithelial cell-specific knockout did not show any overt phenotype (Cognard
53 *et al.*, 2015). Cyst formation has been observed in *Bbs2*$^{-/-}$ and *Bbs4*$^{-/-}$ mice, but again primarily affecting
54 glomeruli (Nishimura *et al.*, 2004; Guo *et al.*, 2011). Loss of *Bbs8* has so far shown to cause the most
55 severe retinal phenotype in mice (Tadenev *et al.*, 2011; Dilan *et al.*, 2018; Schneider *et al.*, 2021), which
56 is not only caused by ciliary defects of photoreceptor cells themselves but also due to ciliary defects in
57 the adjacent retinal pigmental epithelial cells (RPE) (Kretschmer *et al.*, 2019, 2023; Schneider *et al.*,
58 2021). The severity of *Bbs8* loss is likely due to the fact that BBS8 is one of the key components of the
59 BBSome. BBS8 (TTC8) is a tetratricopeptide repeat (TPR) protein with a critical role in planar cell
60 polarity and laterality (May-Simera *et al.*, 2010, 2015). Loss of *Bbs8* leads to changes in the composition
61 of the octameric BBSome complex, where BBS8 is a direct interactor of the scaffold protein BBS9
62 (Zhang *et al.*, 2012).

63 Until now, research into BBS8's function has predominantly focused on embryonic development and
64 ocular health, leaving its specific role in cilia maintenance within the kidney and in preserving kidney
65 architecture and function largely unexplored. In this study, we report on tubular cystic and fibrotic
66 kidney disease in adult mice deficient in *Bbs8*. We further provide evidence for cell death and
67 inflammation in these kidneys. An unbiased proteomic analysis of kidney tissue revealed alterations in
68 protein expression and phosphorylation, including increased levels of HDAC2, which we also found to

69 co-precipitate with BBS8. Increased HDAC2 levels upon loss of *Bbs8* also resulted in deacetylation of
70 ciliary microtubules and impaired ciliary stability, which we suggest might be contributing to BBS
71 pathomechanisms.

72 **Methods**

73 *Mouse lines*

74 *Bbs8*$^{-/-}$ mice have been previously described (Tadenev *et al.*, 2011). All animals were housed and
75 handled, and animal studies conducted, in accordance with approved institutional animal care and use
76 committee procedures. All experiments had ethical approval from the Landesuntersuchungsamt
77 Rheinland-Pfalz and were performed in accordance with institutional guidelines for animal welfare,
78 German animal protection law and the guidelines given by the ARVO Statement for the Use of Animals
79 in Ophthalmic and Vision Research. Animal maintenance and handling were performed in line with the
80 Federation for Laboratory Animal Science Associations (FELASA) recommendations. Animals were
81 housed in a 12 h light/dark cycle with food and water available ad libitum. For the preparation, mice
82 were weighted, followed by cervical dislocation; blood was collected prior to the perfusion of the
83 kidney with PBS through the aorta. Further, other organs and fat tissue were taken and, as the kidney,
84 processed by fixation in 4 % formaldehyde and embedded in paraffin as well as snap-frozen for further
85 tissue analysis. The blood was incubated for 2 h at RT, followed by centrifugation. Serum creatinine
86 levels were measured by the Institute of Clinical Chemistry, University Hospital of Cologne, Germany.

87 *Immunohistology*

88 For histological analysis, tissue was cut into 2-µm-thick sections and deparaffinized by xylene
89 treatment and rehydration in graded ethanol. For PAS staining the sections were stained with 0,9 %
90 periodic acid (cat# 3257.1, Roth) and Schiffsches Reagent (cat#1.09033, Merck) both for 10 min
91 embedded into washing steps with H_2O. Finally, to visualize nuclei in blue, the samples were stained
92 with Mayer's Haematoxylin for 20 s. For the Masson staining the Masson-Goldner's trichrome staining
93 kit (cat#3459, Roth) was used and performed according to the manufacturer instructions. After
94 dehydration of the sections, they were embedded with Histomount (HS-103, National Diagnostics).

95 *Isolation and Immortalization of mouse embryonic fibroblasts*

96 For the isolation of mouse embryonic fibroblasts (MEFs), timed matings were set-up with one male
97 and two females of the desired genotype. At day 13, the pregnant mouse was anesthetized using
98 isoflurane (Piramal Healthcare) followed by a cervical dislocation. The lower abdomen was opened by
99 an abdominal incision to extract the two uterine horns. Embryos were isolated, transferred into a 24-
100 well plate filled with PBS, and the head and the red organs (heart and liver) were removed. The rest of
101 the embryo was placed into a 12-well plate filled with 2 ml ice-cold 0.25 % Trypsin/PBS (diluted from

102 2.5 % Trypsin, Gibco). The embryos were chopped into small pieces and incubated overnight at 4 °C.
103 Then, the trypsin solution was discarded and the remaining Trypsin/tissue mixture was incubated for
104 30 min in a 37 °C water bath. Afterwards of medium (composition: DMEM/Glutamax, 10 % FCS, 1 %
105 sodium pyruvate (100x), 1 % Pen Strep), was added, and the cell suspension was pipetted vigorously
106 up and down to break up the digested tissue into a single cell suspension. After 1 min to allow
107 sedimentation of the remaining tissue, the cell suspension was transferred into a new tube. This step
108 was repeated and afterwards, the cell suspension was filtered through a 100 µm cell-strainer (Corning).
109 Cells were plated and after 24 h, the medium was changed. Immortalization of MEFs was performed
110 as described previously (Todaro and Green, 1963). Briefly, cells are split every three days and seeded
111 with the same cell density. From passage three onwards, cells were seeded on at least two 10 cm
112 culture dishes. After around 15 passages, cells started to regrow. When MEFs were immortalized,
113 frozen back-ups were made.

114 *Cell culture*

115 Human embryonic kidney 293T cells (HEK293T, ATCC®) as well as wildtype and *Bbs8*$^{-/-}$ mouse
116 embryonic fibroblasts were cultivated at 37°C and 5% CO_2. Thereby HEK293T cells were maintained in
117 DMEM + GlutaMAX™ medium (Gibco™) supplemented with 10% fetal bovine serum (FBS, Gibco™) and
118 MEFs in DMEM/F-12 + GlutaMAX™ medium (Gibco™) complemented with 10% FBS and 1% penicillin-
119 streptomycin. All cell lines were tested negative for mycoplasma (PCR Mycoplasma Test Kit I/C,
120 PromoKine). To induce ciliogenesis, cells were grown in serum-free media for 24 h. HEK293T cell
121 transfection was performed with 2x HEBS and 0.25 M $CaCl_2$, thereby 5 µg (IP) or 6 µg (Interactome) of
122 the F.hBBS8 pcDNA6 was used and as control, 5 µg (IP) or 6 µg (Interactome) F.EPS$^{1-225}$ pcDNA6 as
123 negative control protein.

124 *Co-Immunoprecipitation*

125 Co-immunoprecipitation (Co-IP) was performed as previously described (Habbig *et al.*, 2011) using the
126 IP Buffer (20 mM Tris, 1% (v/v) TritonX-100, 50 mM NaCl, 15 mM $Na_4P_2O_7$, 50 mM NaF, pH 7.5)
127 supplemented with inhibitors (44 µg/µl PMSF, 2 mM Na_3VO_4). Input samples were collected, and the
128 remaining samples were incubated with anti-FLAG M2 Beads (A2220, Sigma-Aldrich) for 2 h. Samples
129 were lysed in 2x Laemmli (beads) and 1x Laemmli (input). For proteomic analysis, the IP Buffer was
130 supplemented with cOmplete™ Protease Inhibitor Cocktail (Roche). Samples were ultracentrifugated
131 (45.000 rpm, 45 min, and 4°C) before being lysed with 80% SDS in PBS. Subsequently, samples were
132 reduced with 10 mM dithiothreitol and alkylated 40 mM chloroacetamide.

133

134

135 *Immunofluorescence, Immunochemistry and TUNEL staining*

136 The kidney tissue staining of 4 µm (cilia staining) and 2 µm (other stainings) fixed sections were
137 performed as previously described (Dafinger *et al.*, 2021). The primary antibodies (NF-kB, #8242 Cell
138 Signaling, 1:1000; CD3, MCA-1477 Biorad, 1:100; acetylated Tubulin, T6793 Sigma, 1:1000; Slc12a3,
139 HPA028748, Sigma Aldrich, 1:500; ARL13B, 17711-1-AP ProteinTech, 1:500) were incubated overnight
140 at 4°C, followed by incubation with secondary antibodies. For immunochemistry, the DBA kit (K3468
141 DAKO, 30 min for NF-kB; SK-4105 Vector, 5 min for CD3) was used and samples counterstained with
142 Hematoxylin. For immunofluorescence, fluorophore-coupled antibodies (Jackson ImmunoResearch,
143 1:500: anti-mouse-Cy5, # 715-175-150; anti-rabbit A647, 711-605-152; anti-mouse-Cy3, 715-165-150;
144 and FITC-Lotus Tetragonolobus Lectin (LTL), FL-1321-2; Vector laboratories, 1:500) were used for 1 h
145 at RT, samples were mounted after a short incubation of Hoechst 33342 (ThermoFisher Scientific,
146 1:5000) with ProLong™ Diamond (ThermoFisher Scientific). The DeadEnd™ Fluorometric TUNEL
147 System (Promega) was performed following the manufacturer's instructions, with the exception that
148 the samples were mounted, with a pre-incubation of Hoechst with ProLong™ Diamond. MEFs were
149 cultured on glass coverslips until confluent. Cells were fixed with 4% PFA for 10 min and washed with
150 1x PBS. Samples were quenched with 50 mM NH_4Cl for 10 min, before permeabilisation with 0,3% PBS-
151 TritonX-100 for 20 min. Antibodies were diluted in Fish-Block (0.1 % (w/v) ovalbumin, 0.5 % (w/v) fish
152 gelatine, in PBS), supplemented with 0,3% TritonX-100. The primary antibody (ARL13B 1:800;
153 acetylated Tubulin, 1:800) were incubated overnight at 4°C followed by the secondary antibodies (anti-
154 rabbit 488, A11034 Invitrogen, 1:400; anti-mouse 555, A31570, Invitrogen, 1:400; DAPI, Roth, 1:400).
155 Finally, coverslips were mounted with Fluoromount-G (ThermoFisher, 00-4958-02) and imaged with
156 the Leica microscope CTR6000, with DM6000B Laser and DFC360FX camera. MEF cell images were
157 deconvoluted with the Leica imaging software LASX. Cilia number and length were determined with
158 the open-source Fiji software.

159 *Cyst index analysis*

160 The cyst index was calculated for whole slide images using open-source software for bioimage analysis
161 QuPath (v0.4.0) (Bankhead *et al.*, 2017). Cysts were detected using an Artificial Neural Network-based
162 pixel classifier. Initially detected cysts were filtered for the minimal area of 400 μm^2 and a minimum
163 circularity value of 0.35. Plots were generated using the Plots of Data web app (Postma and
164 Goedhartid, 2019). For statistical analysis, all results were normalized to the control followed by a two-
165 tailed Student's t-test ($p<0.05$).

166

167

168 *Immunoblotting*

169 Confluent grown MEF cells were starved 24 h prior to harvest with 200 µl RIPA buffer (50 mM Tris HCl,
170 150 mM NaCl, 1% (v/v) NP-4O, 0.5% (w/v) Sodium deoxycholate, 0.1% (w/v) SDS), supplemented with
171 1% Halt Protease and Phosphatase Inhibitor Cocktail (Thermo Scientific™) (Brücker *et al.*, 2023). Cells
172 were lysed on ice and sonicated for 2 s. Protein concentration of lysates was determined and 70 µg
173 protein was loaded onto a 10% SDS-PAGE and subsequently transferred to a PVDF-FL membrane
174 (Millipore). Membranes were incubated overnight at 4°C in primary antibodies (Flag, F7425, Sigma-
175 Aldrich, 1:1000; HDAC2, ab32117 Abcam, 1:1000; acetylated Tubulin, T6793 Sigma, 1:1000; Calnexin,
176 10427-2 AP ProteinTech, 1:1000). Secondary antibodies were incubated for 1 h at RT (Li-COR
177 Biosciences IRDye680 and IRDye800 1:10.000: rb680, 925-68073; mm680, 925-68072; rb800, 925-
178 32213). Signals were visualized using the Odyssey Infrared Imaging System 2800 (Li-COR).

179 *Phospho- and proteome analysis*

180 For each biological replicate a quarter of kidney tissue was used and dounced with a Wheaton Dounce
181 tissue grinder in urea buffer (8 M Urea, 50 mM ammonium bicarbonate) supplemented with Halt
182 protease-phosphatase-inhibitor cocktail (Thermo Scientific™). After clearing of the sample (16.000 xg,
183 1 h at 4°C), the lysates were reduced (10 mM dithiothreitol), alkylated (50 mM chloroacetamide) and
184 digested (LysC; 1:75). Samples (800 µg) were diluted to 2 M urea and subjected to tryptic digestion
185 (1:50). After overnight incubation, phosphoenrichment was performed in the CECAD proteomics
186 facility using the Thermo Scientific™ Kit High Select TiO2 Kit (#A32993). All samples were analyzed as
187 well by the CECAD proteomics facility on a Q Exactive Plus Orbitrap mass spectrometer that was
188 coupled to an EASY nLC (both Thermo Scientific™). Peptides were loaded with solvent A (0.1% formic
189 acid in water) onto an in-house packed analytical column (50 cm, 75 µm inner diameter, filled with 2.7
190 µm Poroshell EC120 C18, Agilent). Peptides were chromatographically separated at a constant flow
191 rate of 250 nL/min using the following gradient: 3-5% solvent B (0.1% formic acid in 80 % acetonitrile)
192 within 1.0 min, 5-30% solvent B within 121.0 min, 30-40% solvent B within 19.0 min, 40-95% solvent B
193 within 1.0 min, followed by washing and column equilibration. The mass spectrometer was operated
194 in data-dependent acquisition mode. The MS1 survey scan was acquired from 300-1750 m/z at a
195 resolution of 70,000. The top 10 most abundant peptides were isolated within a 1.8 Th window and
196 subjected to HCD fragmentation at a normalized collision energy of 27%. The AGC target was set to
197 5e5 charges, allowing a maximum injection time of 55 ms. Product ions were detected in the Orbitrap
198 at a resolution of 17,500. Precursors were dynamically excluded for 25.0 s. All mass spectrometric raw
199 data were processed with MaxQuant (Tyanova, Temu and Cox, 2016) (version 2.2.0.0) using default
200 parameters against the UniProt canonical murine database (UP10090, downloaded 20.01.2023) with
201 the match-between-runs option enabled between replicates. Samples were sorted into two parameter

202 groups, either containing the enriched or non-enriched samples. Enriched samples had the
203 phosphorylation (STY) variable modification added, whereas non-enriched samples were quantified by
204 LFQ. A follow-up analysis was done in Perseus 1.6.15 (Tyanova *et al.*, 2016). Results were cleaned up
205 by removing hits from the decoy database, the contaminant list and, in case of non-enriched fractions,
206 those only identified by modified peptides were removed. Afterwards, results were filtered for data
207 completeness in at least one condition and LFQ values (WP) or intensities (PP), imputed using sigma
208 downshift with standard settings. Finally, FDR-controlled two-sided t-tests between sample groups
209 were performed (S0=0, FDR≤0.05) as well as a 1D enrichment using Perseus (version 1.6.15.0).

210 *Interactome*

211 Samples were analyzed by the CECAD Proteomics Facility on an Orbitrap Exploris 480 (Thermo
212 Scientific, granted by the German Research Foundation under INST 1856/71-1 FUGG) mass
213 spectrometer equipped with a FAIMSpro differential ion mobility device that was coupled to an
214 Vanquish neo in trap-and-elute setup (Thermo Scientific). Samples were loaded onto a precolumn
215 (Acclaim 5µm PepMap 300 µ Cartridge) with a flow of 60 µl/min before reverse-flushed onto an in-
216 house packed analytical column (30 cm length, 75 µm inner diameter, filled with 2.7 µm Poroshell
217 EC120 C18, Agilent). Peptides were chromatographically separated with an initial flow rate of 400
218 nL/min and the following gradient: initial 2% B (0.1% formic acid in 80 % acetonitrile), up to 6 % in 3
219 min. Then, flow was reduced to 300 nl/min and B increased to 20% B in 26 min, up to 35% B within 15
220 min and up to 98% solvent B within 1.0 min while again increasing the flow to 400 nl/min, followed by
221 column wash with 98% solvent B and re-equilibration to initial condition. The FAIMS pro was operated
222 at -50V compensation voltage and electrode temperatures of 99.5 °C for the inner and 85 °C for the
223 outer electrode. The mass spectrometer was operated in data-dependent acquisition top 24 mode
224 with MS1 scans acquired from 350 m/z to 1400 m/z at 60k resolution and an AGC target of 300%. MS2
225 scans were acquired at 15 k resolution with a maximum injection time of 22 ms and an AGC target of
226 300% in a 1.4 Th window and a fixed first mass of 110 m/z. All MS1 scans were stored as profile, all
227 MS2 scans as centroid. All mass spectrometric raw data were processed with Maxquant (version 2.4)
228 (Tyanova, Temu and Cox, 2016) using default parameters against the Uniprot HUMAN canonical
229 database (UP5640) with the match-between-runs option enabled between replicates. Follow-up
230 analysis was done in Perseus 1.6.15 (Tyanova *et al.*, 2016). Protein groups were filtered for potential
231 contaminants and insecure identifications. Remaining IDs were filtered for data completeness in at
232 least one group and missing values imputed by sigma downshift (0.3 σ width, 1.8 σ downshift).
233 Afterwards, FDR-controlled two-sided t-tests were performed (S0=0, FDR≤0.05).

234

235

236 *Quantitative real-time PCR*

237 RNA isolation from kidney tissue, one-quarter of a kidney was ground with BeadBeater (Roth) using a
238 Precelly24 with 5.000 rpm two times for 30 s in Tri-Reagent. RNA extraction was performed with the
239 Direct-zol RNA Miniprep kit (Zymo Research) following the manufacturer's instructions, including a
240 DNase1 treatment step. Before the reverse transcription using the High-Capacity cDNA Reverse
241 Transcription kit (Applied Biosystems, 4368814), RNA concentration and sample quality were assessed
242 on a Nanodrop spectrophotometer (Peqlab). mRNA was assessed by SYBR Green (Thermo Scientific™,
243 4309155) qPCR using mHprt1 as endogenous control. Primers are listed in the supplementary table S1.
244 The qPCR experiments were performed on a QuantStudio 12K Flex Real-time PCR System
245 (ThermoFisher Scientific). For data analysis, all results were normalized to the housekeeping gene
246 *Hprt1* using the delta-delta CT followed by a two-tailed Student's t-test ($p<0.05$).

247 *IL-6 Elisa*

248 Mouse IL-6 Uncoated ELISA kit (cat# 88-7064; Invitrogen) was used to measure Interleukin-6
249 concentrations of mouse tissue lysates. If not stated otherwise, the ELISA plate was prepared, and the
250 assay was conducted after manufacturer’s instructions. For all washing steps 1x PBS supplemented
251 with 0.05% Tween™20 was used. To lyse tissue, approx. 10 mg of snap-frozen tissue was cut into small
252 pieces on dry ice before adding 200 µl of lysis buffer (200 mM NaCl, 10 mM Tris-HCl pH=7.4, 5 mM
253 EDTA, 1% NP-40, 1% Halt Protease-Phosphatase inhibitor (Thermo Scientific™). Tissue was
254 homogenized using a Disruptor Genie Digital (Scientific Industries; SI-DD38). Therefore, the tubes were
255 filled halfway with pre-chilled glass beads and the samples were homogenized with eight 1 min runs
256 at 2.640 rpm, placing the samples on ice in between runs. Kidney tissue was additionally homogenized
257 using a pellet pestle, before all lysates were incubated for further 30 min on ice. Samples were spun
258 down at 21.130 x g and 4°C for 10 min, the supernatant was transferred into a fresh reaction tube and
259 protein concentration was determined via BCA assay. Following amounts of protein were loaded in
260 triplicates and incubated overnight at 4°C: Kidney 300 µg; Liver 300 µg; Fat 125 µg. Sulphuric acid (2 N)
261 was used to stop the colorimetric reaction of Avidin-HRP, before measuring the absorbance at 450 nm
262 and 570 nm, for wavelength subtraction, using the TECAN Spark microplate reader (TECAN).

263 *Quantification and statistical analysis*

264 Data are expressed as mean ± standard deviation (SD). All experiments were performed in at least 3
265 independent biological replicates. The data were statistically analysed with GraphPad Prism version
266 9.5.1 unless otherwise mentioned.

267

268

269 **Results**

270 *Cystic kidney disease in Bbs8 knockout mice*

271 To investigate the function of BBS8 in the kidney, we analyzed kidneys of a conventional *Bbs8* knockout
272 mouse line (Tadenev *et al.*, 2011). Kidney tissue did not show any obvious phenotypic alterations by
273 24 weeks, so we continued monitoring the mice until 46 weeks of age. At this age *Bbs8*$^{-/-}$ animals
274 displayed significant obesity, with a body weight approximately 30% higher than in control **(Fig.1 A, B)**,
275 a common BBS phenotype. Remarkably, loss of *Bbs8* significantly affected the kidneys at this age, as
276 indicated by the small increase in kidney weight **(Fig.1 C),** as well as slightly elevated although not
277 significantly altered blood urea levels **(Fig.1 D)**. PAS staining of kidney tissue revealed cyst formation
278 and dilated tubules **(Fig.1 E/F)** and, remarkably, the cystic index used to quantify cyst formation was
279 6-fold higher in *Bbs8*$^{-/-}$ as compared to control mice **(Fig.1 G)**. Further analysis revealed that the size of
280 individual cysts detected in *Bbs8*$^{-/-}$ was similar to dilated tubules and cysts from age-related dilated
281 tubules of control animals **(Supp. Fig.1),** however the number of these cysts was significantly
282 increased. Staining for proximal and distal tubules in the kidney revealed that the majority of cysts
283 originated from distal tubules, as they were positive for Slc12a3 **(Fig.1 H)**. Interestingly, in keeping with
284 the theory that BBS proteins are typically not essential for ciliogenesis per se, but rather for the
285 sustained maintenance of cilia, epithelial cells of kidney tubules in *Bbs8*$^{-/-}$ mice exhibited primary cilia
286 on their apical surface, even within dilated or cystic areas **(Supp. Fig.3)**. Taken together, *Bbs8* knockout
287 mice, in addition to obesity, fatty liver disease, retinal degeneration, and occasional polydactyly,
288 exhibit cystic kidney disease by 46 weeks of age, where cyst formation predominantly originates from
289 the distal tubular segments.

290 *Cell death and fibrosis in cystic kidneys of Bbs8 knockout mice*

291 *Bbs8*$^{-/-}$ kidneys showed a significant increase in fibrosis, as visualized by Masson's trichrome staining,
292 which indicated an accumulation of connective tissue and collagen **(Fig.2 A**; blue color**)**. Further, this
293 staining also showed clusters of inflammatory cells, as seen by aggregation of nuclei **(Fig.2 A**; dark red**)**.
294 Increased TUNEL positive cells indicated increased cell death in *Bbs8*$^{-/-}$ kidneys, while elevated γH2AX
295 levels pointed to DNA damage and genomic instability. Additionally, we observed an accumulation of
296 T-cells (CD3^{+}), as well as an increased nuclear translocation of the NF-κB protein RelA/p65, in particular
297 in inflammation-rich areas, in *Bbs8*$^{-/-}$ kidney tissue **(Fig.2 B)**. mRNA expression analysis revealed an
298 increase of NF-κB *p50* and *p65* transcription **(Fig.2 C)**. Although mRNA expression level of the
299 necroptosis key kinase *Ripk3* was not significantly altered, we detected a significant increase of the
300 pyroptosis markers *Nlrp3* and *GsdmD*. To gain more information on modulators of the ongoing fibrotic
301 change, we also examined interleukin-6 (IL-6) expression with an ELISA assay and found it significantly
302 upregulated specifically in kidney lysates, with only a non-significant increase in fat or liver tissue **(Fig.2**

303 **D)**. Thus, the loss of *Bbs8*, in addition to cyst formation and dilated tubules, leads to an increased rate
304 of cell death in the kidney, elevated expression of genes related to pyroptosis and the inflammasome,
305 as well as to renal fibrosis and inflammation.

306 *Proteomic analyses of Bbs8-deficient kidneys*

307 To gain insights into the mechanisms behind the kidney pathology, we performed unbiased proteomic
308 expression analysis of the whole proteome (WP); **(Fig.3 A)** and a phospho-proteome (PP) **(Fig.3 B)** of
309 lysates from both *Bbs8*$^{-/-}$ and control kidneys. The principal component analysis clearly separated the
310 two genotypes in both datasets **(Supp. Fig.3 A)**. After quality control (QC), we found 2926 proteins in
311 the WP (**Fig.3 A)**. Based on the student's T-test (S0=0; FDR≤0.05), only 10 proteins were significantly
312 up- and 16 significantly downregulated in *Bbs8*$^{-/-}$**.** Analysis of the phospho-proteome identified 6223
313 phosphosites after QC, within a total of 2188 individual proteins **(Fig.3 B)**. From these phosphosites,
314 151 were significantly up- and 1041 significantly down-regulated. GO-term analysis of the significantly
315 regulated PP proteins revealed an enrichment of biological processes related to protein kinase
316 signaling. In general this analysis represents the kidney phenotype of inflammation, ECM remodelling,
317 and cell death **(Fig.3 C)**. Furthermore, consistent with the presence of inflammation **(Fig.2 D/E)**, KEGG
318 pathway analysis of the same protein set indicated enrichment of pathways related to a type II
319 inflammatory phenotype (Th1,2,17 cell differentiation), as well as toll-like receptor signaling **(Fig.3 D)**.
320 Among the differentially expressed proteins within the WP, some were specifically related to
321 cystogenesis and disease progression: here, dynein cytoplasmic 2 heavy chain 1 (DYNC2H1) and
322 dystrobrevin binding protein 1 (DTNBP1) were found to be downregulated in the knockout. Genetic
323 variants in DYNC2H1 are causative for skeletal and retinal ciliopathies, whereas mutations in DTNBP1
324 causes late-onset cystic kidney disease in mice (Monis, Faundez and Pazour, 2017). Over expressed
325 proteins include retinol binding protein 4 (RBP4), uromodulin (UMOD), nucleoporin 98 (NUP98), and
326 histone deacetylase 2 (HDAC2), each of which has a direct association to kidney diseases or ciliary
327 biology **(Supp. Fig.4 B)** (Zaucke *et al.*, 2010; Kobayashi *et al.*, 2017; Endicott and Brueckner, 2018; Xun
328 *et al.*, 2018). To explore the impact of phosphorylation alterations in *Bbs8*$^{-/-}$, we identified candidates
329 that were significantly regulated in both the WP and PP, exhibiting a minimum fold change of 1.5 and
330 showing counter-regulation. These candidates are presented in a hierarchical clustered heat map
331 **(Fig.3 E)**. Remarkably, this included differences in HDAC2 serine (Ser) residues: Ser424 and Ser422/424.
332 Phosphorylation of pSer394 and pSer422, as well as the double phosphorylation of pSer422/424
333 occurred predominantly in the wild type kidney, however in *Bbs8* knockout kidneys we only detected
334 the peptide phosphorylated at pSer424 **(Supp. Fig.3 C)**. Since this protein has been described to
335 suppress ciliogenesis in cancer cells via AuroraA (Kobayashi *et al.*, 2017), HDAC2 is an interesting
336 candidate, which could contribute to the pathogenesis of BBS. It has been suggested previously that
337 BBS proteins protect against HDAC6-mediated ciliary disassembly and loss of *Bbs8* results in increased

338 HDAC6 (Patnaik *et al.*, 2019). In *Bbs8*$^{-/-}$ kidneys, the histone deacetylases HDAC6 and HDAC1 were
339 detected in the WP but, in contrast to HDAC2, not significantly altered. Therefore, we concluded that
340 HDAC2 could indicate a direct mechanistic link between BBS8 and ciliary tubulin deacetylation, as well
341 as ciliary destabilization.

342 *BBS8 co-precipitates with HDAC2*

343 In light of the significant changes in HDAC2 expression and phosphorylation, we sought to identity a
344 direct link between HDAC2 and BBS8. Therefore, we employed two different approaches to investigate
345 whether HDAC2 and BBS8 are part of a common protein complex. First, we expressed exogenous
346 human FLAG-tagged BBS8 in HEK293T cells and we were able to co-precipitate endogenous HDAC2 as
347 detected via immunoblotting **(Fig.4 A)**. Subsequently, we conducted a similar experiment but analysed
348 the co-precipitated proteins using MS/MS. The principal component analysis clearly separated the
349 F.hBBS8 pulldown from the control **(Supp. Fig.4 A, Supp. Tab. 2)**. We identified 1146 proteins of which
350 981 were potential significant BBS8 interactors **(Fig.4 B)**. Among those were not only many known
351 members of the BBSome (BBS1, BBS2, BBS4, BBS5, BBS7, BBS9) and the chaperonin complex (CCT6A,
352 CCT5, CCT3, CCT2, TCP1, CTT8, CCT4 and CCT7), but also HDAC2. Additional protein groups shown to
353 interact with BBS8 are heat shock binding proteins and proteins related to the Wnt signaling pathway
354 **(Supp. Fig.4 B)**. To investigate this further we compared the list of putative interactors with the
355 published CiliaCarta proteins (Van Dam *et al.*, 2019) **(Fig.4 C)** and found a total of 67 ciliary proteins
356 co-precipitating with BBS8. Comparing the potential BBS8 interactors with significantly differential
357 expressed targets of the WP results in only four candidates, HDAC2 and 3 additional proteins (AGO2,
358 NUP98 and MTHFD1; **Supp. Fig.4 C**).

359 *Increased levels of HDAC2 in Bbs8 deficient cells affects ciliary tubulin acetylation*

360 We could confirm an increased expression of HDAC2 in lysates from mouse embryonic fibroblasts
361 (MEFs) generated from *Bbs8*$^{-/-}$ and matched control mice by immunoblotting **(Fig.4 D)**. This suggests
362 that enhanced HDAC2 expression in *Bbs8*$^{-/-}$ mice might not be restricted to the kidney, but represents
363 a mechanism relevant in other tissues as well. In parallel to immunoblotting, we performed qPCRs,
364 which revealed an upregulation of *Hdac2* mRNA in these cells, indicating that enhanced transcription
365 contributes to the increased levels of HDAC2 expression **(Fig.4 E)**. Since MEFs typically exhibit high
366 levels of ciliation and HDAC2 might be similar to HDAC6 in terms of affecting ciliary disassembly, we
367 analyzed the number and length of cilia in *Bbs8*$^{-/-}$ and control MEFs. Quantification of cilia number and
368 length via ARL13B staining revealed no significant difference in serum starved MEFs **(Fig.4 F),** similar
369 to our findings in the kidney of *Bbs8*$^{-/-}$ mice. Since HDAC2, similar to HDAC6, might negatively regulate
370 acetylation of alpha tubulin within the ciliary axoneme, we co-stained the ciliary membrane marker
371 ARL13B with acetylated tubulin. Quantification revealed that a significant number of cilia in the *Bbs8*$^{-/-}$

372 cells visualized by ARL13B staining did not exhibit labelling for acetylated tubulin **(Fig.4 G)**. Strikingly,
373 we could confirm this reduced acetylation of ciliary tubulin in the kidney tissue of *Bbs8*$^{-/-}$ mice **(Fig.4**
374 **H)**. In summary, the finding of high HDAC2 levels and reduced acetylation in cilia of both, *Bbs8*$^{-/-}$ kidney
375 epithelial cells *in vivo* and in *Bbs8*$^{-/-}$ MEFs, aligns perfectly with the previously described positive effect
376 of HDAC inhibition in ADPKD zebrafish and mouse models (Cao *et al.*, 2009), suggesting a potentially
377 relevant therapeutic option.

378 **Discussion**

379 In this work, we describe the occurrence of a tubular cystic kidney disease in a mouse model with a
380 knockout of a *Bbs* gene. Notably, these animals have long been known to exhibit symptoms such as
381 obesity, polydactyly and blindness. The ocular phenotype of *Bbs8*$^{-/-}$ mice has been studied in great
382 detail, however the renal phenotype has not been previously examined. Here, we describe a relatively
383 late-occurring cystic fibrotic kidney disease in homozygous mouse knockouts, accurately reflecting the
384 patient renal manifestation. The kidney phenotype in BBS patients is variable with kidneys showing
385 parenchymal cysts, medullary and most often corticomedullary cysts, but also renal fibrosis, unilateral
386 agenesis or dysplastic kidneys (Beales *et al.*, 1999; Putoux *et al.*, 2012; Elawad *et al.*, 2022). However,
387 these phenotypes are highly variable among families and could be caused by the type of mutations
388 (Putoux *et al.*, 2012). In general, kidney disease in BBS patients is diagnosed in approximately 25% of
389 cases, through the fact that many patients do not undergo any specific kidney examination and thereby
390 kidney disease might not be recognized (Beales *et al.*, 1999).

391 It was the identification of BBS8 mutations that first suggested that the BBS phenotype might be
392 attributed to defective primary cilia (Ansley *et al.*, 2003). The loss of *Bbs8* causes a much more severe
393 phenotype than other patient mutations, which could be the reason why BBS8 variants are rare among
394 patients (Stoetzel *et al.*, 2006). Consistently, the phenotype of *Bbs8* deficient mice is likely the most
395 severe among BBS mouse models. Kidney phenotypes have been observed in *Bbs2*, *Bbs4* or *Bbs10*
396 knockout mice where the knockout primarily affected glomeruli and podocytes with indirect systemic
397 effects on tubular cells (Nishimura *et al.*, 2004; Guo *et al.*, 2011; Cognard *et al.*, 2015). The at hand
398 study now describes a tubular cystic kidney phenotype in a BBS mouse model which will allow to
399 conduct preclinical studies on tubular cystic kidney disease in a BBS genetic context.

400 Regarding the precise mechanisms underlying kidney disease in *Bbs8*$^{-/-}$, our proteomic analyses
401 revealed a number of interesting candidates, which potentially contribute to kidney
402 pathomechanisms. The downregulation of DTNBP1, a subunit of the biogenesis of lysosome-related
403 organelles complex-1 (BLOC-1), could contribute to the kidney phenotype as it is known to cause cystic
404 kidney disease upon mutation in mice by reducing ciliary expression of polycystin-2 (Monis, Faundez
405 and Pazour, 2017). In addition, we observed decreased levels of DYNC2H1 in *Bbs8*$^{-/-}$ mice. DYNC2H1 is

406 a known subunit of the IFT-dynein motor, which drives retrograde IFT-rafts and plays a role in the
407 formation of the transition zone. Mutations lead to the skeletal ciliopathies Jeune asphyxiating thoracic
408 dystrophy and short-rib polydactyly and also to non-syndromic retina degeneration (Jensen *et al.*,
409 2018; Vig *et al.*, 2020). Reduced levels of DYNC2H1 in *Bbs8*$^{-/-}$ could contribute both to the renal and
410 retinal phenotype (Vig *et al.*, 2020). Another interesting finding is the increased abundance of UMOD,
411 a protein expressed in renal primary cilia. Variants of the UMOD gene lead to autosomal-dominant
412 tubulointerstitial kidney diseases (Zaucke *et al.*, 2010). Additionally, UMOD is found to be involved in
413 renal cyst formation in human kidney biopsies, which is in line with the upregulation in *Bbs8*$^{-/-}$ (Gresh
414 *et al.*, 2004). The proteomic analysis also revealed increased expression of RBP4 in kidney tissue.
415 Increased RBP4 has been suggested as a biomarker for renal damage and proteinuria (Ratajczyk *et al.*,
416 2022), which has also been suggested for UMOD (Thielemans *et al.*, 2023). Therefore, further studies
417 need to address whether serum or urinary RBP4 or UMOD levels could be used as a potential biomarker
418 for kidney disease onset and progression in BBS patients (Xun *et al.*, 2018; Swa *et al.*, 2022), similar to
419 what has been suggested for UMOD in ADPKD (Cansever *et al.*, 2021). In addition to the individual
420 expression and phosphorylation analysis, comparing the unbiased proteome- and phosphoproteome
421 with the BBS8 interactome unearthed further interesting candidates. Here, in particular four genes
422 showed up in all three analyses. Among those candidates, NUP98 is particularly notable, which is a
423 nucleoporin that plays a crucial role in size-selective diffusion at the base of cilia (Endicott and
424 Brueckner, 2018). AGO-2 has also been described at the base of cilia in astrocytes and could play a role
425 in BBS (Moser, Fritzler and Rattner, 2011), while *Mthfd1*, which codes for a protein in folate
426 metabolism, has not yet been associated with cilia or cystic kidneys.

427 Based on the role of tubulin acetylation in cilia and fundamental previous studies on HDAC6 in regard
428 to ciliary disassembly (Pugacheva *et al.*, 2007), we focused on HDAC2. HDAC2 showed increased
429 expression in our proteome analyses and we also found a strong interaction between HDAC2 and BBS8
430 upon IP. In addition to its nuclear functions, HDAC2 could regulate the stability and, thus, dynamics of
431 cilia through the deacetylation of tubulin, similar to HDAC6. HDAC6 is enriched at the centrosome and
432 basal body, where it catalyzes the deacetylation of alpha-tubulin and, therefore, plays a role in the
433 disassembly of primary cilia (Ran *et al.*, 2015). This process can be prevented by BBS proteins through
434 the recruitment of Inversin to the ciliary base (Patnaik *et al.*, 2019). In general, HDAC6 is activated by
435 phosphorylation after HEF1-dependent activation of the oncogenic Aurora A (AurA) kinase (Pugacheva
436 *et al.*, 2007). We found increased levels of HDAC2 in *Bbs8*$^{-/-}$ kidneys, as well as *Bbs8*$^{-/-}$ MEFs and
437 observed diminished acetylation of tubulin inside cilia on *Bbs8* knockout cells. This might result in a
438 subtle defect in ciliary dynamics.

439 Even though we found differences in HDAC2, we did not expect cilia to be severely affected. This would
440 not be in line with data from other BBS genes, nor would it explain the late-onset phenotype we

441 observed. Similarly, our findings related to cell death, fibrosis, and inflammation are relatively
442 moderate. Given the late onset and slow progression of kidney disease in this model, we would not
443 expect the loss of *Bbs8* to result in massive overactivity of any specific cell death pathway. Our results
444 suggest that cell death and inflammation are rather secondary processes that, while present, do not
445 constitute the primary cause of the kidney disease. Since the activity of HDAC2 is regulated by
446 phosphorylation through casein kinase II and the regulation of expression levels by proteasomal
447 degradation (Eom and Kook, 2015), it might open potential options for pharmacologically interventions
448 targeting HDAC2-dependent deacetylation. To what extent the nuclear functions of HDAC2 are also
449 altered and contribute to the pathogenesis of kidney disease requires further investigation.

450

451 **Figure legends:**

452 **Figure 1. *Bbs8*$^{-/-}$ mice develop late-onset cystic kidney disease.**

453 **(A/B)** Image of 46-week-old control (*Bbs8*$^{+/+}$) and *Bbs8*$^{-/-}$ mice, and the body weight indicated
454 significant obesity in knockout animals (n=4). **(C)** Kidney weight of the mice did not significantly alter
455 between both mouse models. **(D)** Serum urea of control and *Bbs8*$^{-/-}$ mice show an increasing trend
456 (n=4). **(E/F)** PAS staining of the whole kidney in control and *Bbs8*$^{-/-}$ animals; Scale bar: 1 mm. The area
457 in the zoom-in comprises the cortex and medullary area of the kidney; Scale bar: 200 µm. **(G)** Cyst
458 index described in a cyst-to-tissue area ratio, normalised to control animals. **(H)** Kidney image for distal
459 tubules (Slc12a3, magenta) and proximal tubules (LTL, green) show cyst formation in clustered distal
460 tubules; Scale bar: 500 µm.

461 **Figure 2. Cell death, fibrosis and inflammation in *Bbs8*$^{-/-}$ kidneys.**

462 Representative microscopic images of control and Bbs8$^{-/-}$ mice for **(A)** Masson's trichrome stain; Scale
463 bar: 300 µm **(B)** TUNEL staining and yH2AX, Scale bar: 100 µm; CD3^{+} and NF-kB expression, Scale bar:
464 300 µm. Arrowheads, indicates positive events. **(C)** Quantitative real-time PCR of *NF-kB/p50*, *RelA/p65*
465 and inflammasome genes in control and *Bbs8*$^{-/-}$ kidney samples (n=4). Statistical analysis was
466 performed using a two-sided student's *T-test* (*p*-value: <0.001***; 0.002**; 0.033*; ns = 0.12). **(D)** IL-6
467 Elisa performed for kidney, liver and fat tissue.

468 **Figure 3. Proteomic analysis hints toward HDAC2 as putative key player in *Bbs8*$^{-/-}$ kidneys.**

469 Scatter blot of **(A)** whole proteome (WP) or **(B)** phosphoproteome (PP) marked with significantly
470 (FDR≤0.05) up- (yellow) or downregulated (cyan) proteins. Labelled HDAC proteins and their activator
471 kinase CK2 as well as further interesting candidates. **(C/D)** GOBP and KEGG pathway based on 1D-
472 enrichment of the proteins found in the PP, separated for up- (yellow) and downregulation (cyan). Top

473 10 candidates are ordered by p-values within the groups. **(E)** Clustered hierarchal heat map based on
474 log_2 LFQ intensities and fold change=1.5 of WP and PP proteins wither their phosphorylation position
475 in the protein which are significantly, and counter regulated.

476 **Figure 4. HDAC2 interacts with BBS8 and increased levels affect ciliary tubulin acetylation**

477 **(A)** Co-IP from HEK293T cells, overexpressing F.hBBS8 or F.hEPS as control, show an interaction of BBS8
478 with HDAC2. Protein extracts (Lysate) were immunoprecipitated with α-Flag (IP) and detected and
479 detected with α-Flag (F.hBBS8 ~65 kDa, F.hEPS ~30 kDa) and α-HDAC2 (55 kDa) (n=3). **(B)** Scatter blot
480 of BBS8 interactors, performed in HEK293T cells overexpressing F.hBBS8 or F.hEPS as control. Potential
481 Interactors (FDR≤0.05), marked in magenta, revealed HDAC2 as an interactor of BBS8. **(C)**
482 Venn-Diagram showing the overlap between the BBS8 interactors and the published CiliaCarta**. (D)**
483 Control or *Bbs8*$^{-/-}$ mouse embryonic fibroblasts (MEFs) were immunoblotted against HDAC2 (~55 kDa),
484 acetylated Tubulin (~55 kDa). All samples were normalized to Calnexin (~96 kDa). **(E)** qPCR of *Hdac2* in
485 control and *Bbs8*$^{-/-}$ MEFs samples (n=3). Statistical analysis was performed using a two-sided student's
486 *T-test* (*p*-value: <0.001***; 0.002**; 0.033*; ns = 0.12). **(F)** Representative images of cultured MEF
487 *Bbs8* knockout and control cells, stained with the cilia marker ARL13B and counterstained with DAPI;
488 Scale bar: 20 µm. Primary cilia are quantified for the number and length of cilia (n=4). **(G)** Primary cilia
489 count in MEFs, which are ARL13B and acetylated Tubulin (ac-Tub) positive. Representative images of
490 primary cilia in MEFs with the overlay of marker ARL13B and ac-Tub, counterstained with DAPI; Scale
491 bar: 10 µm. **(H)** ARL13B (green) and acetylated tubulin (magenta) staining of cilia in kidney tissue of
492 control and Bbs8$^{-/-}$ mice and the ratio of ARL13B and acetylated tubulin positive cilia (n=3). All data in
493 this figure were statistically analysed using an unpaired Student's *t-test* (*p*-value: <0.001***; 0.002**;
494 0.033*; ns = 0.12).

495 Supplementary Figure 1. **Small-cyst formation in *Bbs8*$^{-/-}$ kidney.**

496 **(A)** Measured cyst area depicted as jittered dots with the mean as a horizontal line. The values are
497 plotted on a log_{10} scale. The overall number of cysts was scientifically increased in knockout animals.
498 The data were statistically analysed using a two-sided student's *t-test* (*p*-value: <0.001***; 0.002**;
499 0.033*; ns = 0.12).

500 Supplementary Figure 2**. The occurrence of cilia in conventional *Bbs8 knockout is not altered.***

501 **(A)** Cilia staining with ARL13B showed no difference in ciliation between control and *Bbs8*$^{-/-}$ kidney;
502 Scale bar: 50 µm; Zoom-in scale bar: 25 µm.

503 Supplementary Figure 3. ***Additional analyses based on the proteomic data***

504 **(A)** Principal component analysis (PCA) plots of the protein expression data of control and *Bbs8*$^{-/-}$
505 kidney samples. Depicted are the first two principal components for either whole proteome (WP) or
506 phosphoproteome (PP). The axes represent the percentages of variation explained by the principal
507 components. **(B)** Table of significantly up- and downregulated proteins of the WP. **(C)** Table of different
508 expressed HDAC2 residues with their related phosphosites and regulation. **(D)** KEGG, GOCC and GOMF
509 of WP **(E)** GOMF and GOCC of PP. All GO-terms based on 1D-enrichment, separated for up- (yellow)
510 and downregulation (cyan). Ordered by p-values within the groups**.**

511 Supplementary Figure 4. **Additional analyses of the interactome data**

512 **(A)** Principal component analysis (PCA) plots of the protein expression data of F.GFP and F.hBBS8,
513 shown with the first two principal components. The axes represent the percentages of variation
514 explained by the principal components. **(B)** Scatter plot of different protein clusters expressed in the
515 BBS8 interactome for different GO-terms: BBSome, chaperonin-containing T-complex, heat shock
516 protein binding and Wnt signaling pathway. **(C)** Venn-Diagram of BBS8 interaction partners (986) with
517 the significant candidates of the WP (26) showed an overlap of 4 proteins.

518 Supplementary Figure 5. **Original data: full-sized immunoblots.**

519 Original western blots only cropped to gel size **(A)** of Figure 4 A and **(B)** of Figure 4 E.

520

521 **Acknowledgments**

522 We extend our gratitude to Angelika Köser, Serena Greco-Torres and Stefanie Keller for their valuable
523 technical assistance. We also wish to acknowledge the great support provided by the CECAD imaging
524 facility and the CECAD proteomics facility. Furthermore, we want to convey our appreciation to all the
525 individuals in our research group and numerous members of the SFB1403 for their meaningful
526 discussions and support.

527 Funding: This study was supported by the German Research Foundation (DFG; SFB1403, project
528 number 414786233, A09 to B.S. and T.B.; and FOR5547 to HMS, DW, and BS, project number
529 503306912, under Germany's Excellence Strategy – EXC2151 – Project-ID 390873048 (to D.W.), and
530 WA 3382/8-1 – Project-ID 513767027 (to D.W.). B.S. was also supported by the German Federal
531 Ministry of Research and Education (BMBF grant 01GM1515; NEOCYST consortium) and by the
532 European Union (TheraCil). D.W. was also supported by the Else Kröner Fresenius Foundation
533 (2021.EKFSE.53). P.M. was supported by the Studienstiftung des Deutschen Volkes. The CECAD
534 proteomics facility was supported by the large instrument grant INST 1856/71-1 FUGG by the German
535 Research Foundation (DFG Großgeräteantrag).

References

Ansley, S. J. *et al.* (2003) 'Basal body dysfunction is a likely cause of pleiotropic Bardet-Biedl syndrome', *Nature*, 425(6958), pp. 628–633. doi: 10.1038/NATURE02030.

Bankhead, P. *et al.* (2017) 'QuPath: Open source software for digital pathology image analysis', *Scientific Reports 2017 7:1*, 7(1), pp. 1–7. doi: 10.1038/s41598-017-17204-5.

Bardet, G. (1995) 'On congenital obesity syndrome with polydactyly and retinitis pigmentosa (a contribution to the study of clinical forms of hypophyseal obesity). 1920.', *Obesity research*, 3(4), pp. 387–99. Available at: http://www.ncbi.nlm.nih.gov/pubmed/8521156 (Accessed: 17 October 2019).

Beales, P. L. *et al.* (1999) 'New criteria for improved diagnosis of Bardet-Biedl syndrome: results of a population survey', *Journal of Medical Genetics*, 36(6), p. 437. doi: 10.1136/jmg.36.6.437.

Bentley-Ford, M. R. *et al.* (2021) 'A mouse model of BBS identifies developmental and homeostatic effects of BBS5 mutation and identifies novel pituitary abnormalities', *Human molecular genetics*, 30(3–4), pp. 234–246. doi: 10.1093/HMG/DDAB039.

Biedl, A. (1995) 'A pair of siblings with adiposo-genital dystrophy. 1922.', *Obesity research*, 3(4), p. 404. Available at: http://www.ncbi.nlm.nih.gov/pubmed/8521158 (Accessed: 17 October 2019).

Brücker, L. *et al.* (2023) 'The actin-bundling protein Fascin-1 modulates ciliary signalling', *Journal of Molecular Cell Biology*, 15(4), p. 22. doi: 10.1093/JMCB/MJAD022.

Cansever, H. N. *et al.* (2021) 'Serum uromodulin levels, MR imaging findings, and their relationship with eGFR-based CKD staging in ADPKD patients', *International urology and nephrology*, 53(7), pp. 1383–1389. doi: 10.1007/S11255-020-02730-5.

Cao, Y. *et al.* (2009) 'Chemical modifier screen identifies HDAC inhibitors as suppressors of PKD models', *Proceedings of the National Academy of Sciences of the United States of America*, 106(51), pp. 21819–21824. doi: 10.1073/PNAS.0911987106.

Cognard, N. *et al.* (2015) 'Comparing the Bbs10 complete knockout phenotype with a specific renal epithelial knockout one highlights the link between renal defects and systemic inactivation in mice', *Cilia*, 4. Available at: https://ciliajournal.biomedcentral.com/articles/10.1186/s13630-015-0019-8 (Accessed: 30 March 2021).

Dafinger, C. *et al.* (2021) 'Targeted deletion of Ruvbl1 results in severe defects of epidermal development and perinatal mortality', *Molecular and Cellular Pediatrics*, 8(1). doi: 10.1186/S40348-021-00111-1.

Van Dam, T. J. P. *et al.* (2019) 'CiliaCarta: An integrated and validated compendium of ciliary genes', *PLoS ONE*, 14(5). doi: 10.1371/JOURNAL.PONE.0216705.

Davis, R. E. *et al.* (2007) 'A knockin mouse model of the Bardet-Biedl syndrome 1 M390R mutation has cilia defects, ventriculomegaly, retinopathy, and obesity', *Proceedings of the National Academy of Sciences of the United States of America*, 104(49), pp. 19422–19427. doi: 10.1073/PNAS.0708571104.

Dilan, T. L. *et al.* (2018) 'Bardet-Biedl syndrome-8 (BBS8) protein is crucial for the development of outer segments in photoreceptor neurons.', *Human molecular genetics*, 27(2), pp. 283–294. doi: 10.1093/hmg/ddx399.

Elawad, O. A. M. A. *et al.* (2022) 'Bardet–Biedl syndrome: a case series', *Journal of Medical Case Reports*, 16(1), pp. 1–9. doi: 10.1186/S13256-022-03396-6/FIGURES/4.

Endicott, S. J. and Brueckner, M. (2018) 'NUP98 Sets the Size-Exclusion Diffusion Limit through the Ciliary Base', *Current biology : CB*, 28(10), pp. 1643-1650.e3. doi: 10.1016/J.CUB.2018.04.014.

Eom, G. H. and Kook, H. (2015) 'Role of histone deacetylase 2 and its posttranslational modificationsin cardiac hypertrophy', *BMB Reports*, 48(3), p. 131. doi: 10.5483/BMBREP.2015.48.3.242.

Fan, C.-M. and Tessier-Lavigne, M. (1994) 'Patterning of mammalian somites by surface ectoderm and notochord: Evidence for sclerotome induction by a hedgehog homolog', *Cell*, 79(7), pp. 1175–1186. doi: 10.1016/0092-8674(94)90009-4.

Fath, M. A. *et al.* (2005) 'Mkks-null mice have a phenotype resembling Bardet-Biedl syndrome', *Human molecular genetics*, 14(9), pp. 1109–1118. doi: 10.1093/HMG/DDI123.

Forsythe, E. and Beales, P. L. (2013) 'Bardet–Biedl syndrome', *European Journal of Human Genetics*, 21(1), pp. 8–13. doi: 10.1038/ejhg.2012.115.

Garcia-Gonzalo, F. R. and Reiter, J. F. (2017) 'Open Sesame: How Transition Fibers and the Transition Zone Control Ciliary Composition', *Cold Spring Harbor perspectives in biology*, 9(2). doi: 10.1101/CSHPERSPECT.A028134.

Gopalakrishnan, J. *et al.* (2023) 'Emerging principles of primary cilia dynamics in controlling tissue organization and function', *The EMBO Journal*, p. e113891. doi: 10.15252/EMBJ.2023113891.

Gresh, L. *et al.* (2004) 'A transcriptional network in polycystic kidney disease', *EMBO Journal*, 23(7), pp. 1657–1668. doi: 10.1038/SJ.EMBOJ.7600160/SUPPL_FILE/EMBJ7600160-SUP-0006.PDF.

Guo, D. F. *et al.* (2011) 'Inactivation of Bardet-Biedl syndrome genes causes kidney defects', *American Journal of Physiology - Renal Physiology*, 300(2), p. F574. doi: 10.1152/AJPRENAL.00150.2010.

Habbig, S. *et al.* (2011) 'NPHP4, a cilia-associated protein, negatively regulates the Hippo pathway', *The Journal of cell biology*, 193(4), pp. 633–642. doi: 10.1083/JCB.201009069.

Hildebrandt, F., Benzing, T. and Katsanis, N. (2011) 'Ciliopathies', *The New England journal of medicine*, 364(16), pp. 1533–1543. doi: 10.1056/NEJMRA1010172.

Hildebrandt, F. and Zhou, W. (2007) 'Nephronophthisis-associated ciliopathies.', *Journal of the American Society of Nephrology : JASN*, 18(6), pp. 1855–71. doi: 10.1681/ASN.2006121344.

Jensen, V. L. *et al.* (2018) 'Role for intraflagellar transport in building a functional transition zone', *EMBO reports*, 19(12). doi: 10.15252/EMBR.201845862.

Kobayashi, T. *et al.* (2017) 'HDAC2 promotes loss of primary cilia in pancreatic ductal adenocarcinoma', *EMBO reports*, 18(2), pp. 334–343. doi: 10.15252/EMBR.201541922.

Kretschmer, V. *et al.* (2019) 'Progressive Characterization of Visual Phenotype in Bardet-Biedl Syndrome Mutant Mice', *Investigative ophthalmology & visual science*, 60(4), pp. 1132–1143. doi: 10.1167/IOVS.18-25210.

Kretschmer, V. *et al.* (2023) 'Deletion of IFT20 exclusively in the RPE ablates primary cilia and leads to retinal degeneration', *PLoS biology*, 21(12). doi: 10.1371/JOURNAL.PBIO.3002402.

Kulaga, H. M. *et al.* (2004) 'Loss of BBS proteins causes anosmia in humans and defects in olfactory cilia structure and function in the mouse', *Nature genetics*, 36(9), pp. 994–998. doi: 10.1038/NG1418.

Laurence, J. Z. and Moon, R. C. (1995) 'Four cases of "retinitis pigmentosa" occurring in the same family, and accompanied by general imperfections of development. 1866.', *Obesity research*, 3(4), pp. 400–3. Available at: http://www.ncbi.nlm.nih.gov/pubmed/8521157 (Accessed: 17 October 2019).

Loktev, A. V. *et al.* (2008) 'A BBSome Subunit Links Ciliogenesis, Microtubule Stability, and Acetylation', *Developmental Cell*, 15(6), pp. 854–865. doi: 10.1016/j.devcel.2008.11.001.

May-Simera, H. L. *et al.* (2010) 'Bbs8, together with the planar cell polarity protein Vangl2, is required to establish left-right asymmetry in zebrafish', *Developmental biology*, 345(2), pp. 215–225. doi: 10.1016/J.YDBIO.2010.07.013.

May-Simera, H. L. *et al.* (2015) 'Ciliary proteins Bbs8 and Ift20 promote planar cell polarity in the cochlea', *Development (Cambridge, England)*, 142(3), pp. 555–566. doi: 10.1242/DEV.113696.

McConnachie, D. J., Stow, J. L. and Mallett, A. J. (2021) 'Ciliopathies and the Kidney: A Review', *American journal of kidney diseases : the official journal of the National Kidney Foundation*, 77(3), pp. 410–419. doi: 10.1053/J.AJKD.2020.08.012.

Monis, W. J., Faundez, V. and Pazour, G. J. (2017) 'BLOC-1 is required for selective membrane protein trafficking from endosomes to primary cilia', *The Journal of cell biology*, 216(7), pp. 2131–2150. doi: 10.1083/JCB.201611138.

Moser, J. J., Fritzler, M. J. and Rattner, J. B. (2011) 'Repression of GW/P body components and the RNAi microprocessor impacts primary ciliogenesis in human astrocytes', *BMC cell biology*, 12. doi: 10.1186/1471-2121-12-37.

Munsterberg, A. E. *et al.* (1995) 'Combinatorial signaling by Sonic hedgehog and Wnt family members induces myogenic bHLH gene expression in the somite.', *Genes & Development*, 9(23), pp. 2911–2922. doi: 10.1101/gad.9.23.2911.

Mykytyn, K. *et al.* (2004) 'Bardet-Biedl syndrome type 4 (BBS4)-null mice implicate Bbs4 in flagella formation but not global cilia assembly', *Proceedings of the National Academy of Sciences of the United States of America*, 101(23), pp. 8664–8669. doi: 10.1073/PNAS.0402354101.

Nachury, M. V. *et al.* (2007) 'A Core Complex of BBS Proteins Cooperates with the GTPase Rab8 to Promote Ciliary Membrane Biogenesis', *Cell*, 129(6), pp. 1201–1213. doi: 10.1016/j.cell.2007.03.053.

Nishimura, D. Y. *et al.* (2004) 'Bbs2-null mice have neurosensory deficits, a defect in social dominance, and retinopathy associated with mislocalization of rhodopsin', *Proceedings of the National Academy of Sciences of the United States of America*, 101(47), pp. 16588–16593. doi: 10.1073/PNAS.0405496101.

Patnaik, S. R. *et al.* (2019) 'Bardet–Biedl Syndrome proteins regulate cilia disassembly during tissue maturation', *Cellular and Molecular Life Sciences*, 76(4), pp. 757–775. doi: 10.1007/s00018-018-2966-x.

Pazour, G. J. and Bloodgood, R. A. (2008) 'Targeting Proteins to the Ciliary Membrane', *Current Topics in Developmental Biology*, 85, pp. 115–149. doi: 10.1016/S0070-2153(08)00805-3.

Postma, M. and Goedhartid, J. (2019) 'PlotsOfData-A web app for visualizing data together with their summaries'. doi: 10.1371/journal.pbio.3000202.

Pourquié, O. *et al.* (1996) 'Lateral and Axial Signals Involved in Avian Somite Patterning: A Role for BMP4', *Cell*, 84(3), pp. 461–471. doi: 10.1016/S0092-8674(00)81291-X.

Pugacheva, E. N. *et al.* (2007) 'HEF1-dependent Aurora A activation induces disassembly of the primary cilium', *Cell*, 129(7), pp. 1351–1363. doi: 10.1016/J.CELL.2007.04.035.

Putoux, A. *et al.* (2012) 'Phenotypic variability of Bardet-Biedl syndrome: focusing on the kidney', *Pediatric Nephrology*, 27(1), pp. 7–15. doi: 10.1007/s00467-010-1751-3.

Rahmouni, K. *et al.* (2008) 'Leptin resistance contributes to obesity and hypertension in mouse models of Bardet-Biedl syndrome', *The Journal of clinical investigation*, 118(4), pp. 1458–1467. doi: 10.1172/JCI32357.

Ran, J. *et al.* (2015) 'Deacetylation of α-tubulin and cortactin is required for HDAC6 to trigger ciliary

disassembly', *Scientific reports*, 5. doi: 10.1038/SREP12917.

Ratajczyk, K. *et al.* (2022) 'The Clinical Significance of Urinary Retinol-Binding Protein 4: A Review', *International Journal of Environmental Research and Public Health*, 19(16). doi: 10.3390/IJERPH19169878/S1.

Reiter, J. F., Blacque, O. E. and Leroux, M. R. (2012) 'The base of the cilium: roles for transition fibres and the transition zone in ciliary formation, maintenance and compartmentalization', *EMBO Reports*, 13(7), p. 608. doi: 10.1038/EMBOR.2012.73.

Reiter, J. F. and Leroux, M. R. (2017) 'Genes and molecular pathways underpinning ciliopathies', *Nature Reviews Molecular Cell Biology 2017 18:9*, 18(9), pp. 533–547. doi: 10.1038/nrm.2017.60.

Schneider, S. *et al.* (2021) 'Loss of Ciliary Gene Bbs8 Results in Physiological Defects in the Retinal Pigment Epithelium', *Frontiers in Cell and Developmental Biology*, 9, p. 607121. doi: 10.3389/FCELL.2021.607121/FULL.

Seo, S. *et al.* (2009) 'Requirement of Bardet-Biedl syndrome proteins for leptin receptor signaling', *Human molecular genetics*, 18(7), pp. 1323–1331. doi: 10.1093/HMG/DDP031.

Seo, S. *et al.* (2010) 'BBS6, BBS10, and BBS12 form a complex with CCT/TRiC family chaperonins and mediate BBSome assembly.', *Proceedings of the National Academy of Sciences of the United States of America*, 107(4), pp. 1488–93. doi: 10.1073/pnas.0910268107.

Stoetzel, C. *et al.* (2006) 'BBS8 is rarely mutated in a cohort of 128 Bardet-Biedl syndrome families', *Journal of human genetics*, 51(1), pp. 81–84. doi: 10.1007/S10038-005-0320-2.

Swa, H. L. F. *et al.* (2022) 'Evaluating Serum RBP4 as an Auxiliary Biomarker for CKDu Diagnosis', *Kidney and Dialysis 2022, Vol. 2, Pages 576-587*, 2(4), pp. 576–587. doi: 10.3390/KIDNEYDIAL2040052.

Tadenev, A. L. D. *et al.* (2011) 'Loss of Bardet-Biedl syndrome protein-8 (BBS8) perturbs olfactory function, protein localization, and axon targeting', *Proceedings of the National Academy of Sciences of the United States of America*, 108(25), pp. 10320–10325. doi: 10.1073/PNAS.1016531108.

Thielemans, R. *et al.* (2023) 'Unveiling the Hidden Power of Uromodulin: A Promising Potential Biomarker for Kidney Diseases', *Diagnostics (Basel, Switzerland)*, 13(19). doi: 10.3390/DIAGNOSTICS13193077.

Todaro, G. J. and Green, H. (1963) 'Quantitative studies of the growth of mouse embryo cells in culture and their development into established lines', *The Journal of cell biology*, 17(2), pp. 299–313. doi: 10.1083/JCB.17.2.299.

Tyanova, S. *et al.* (2016) 'The Perseus computational platform for comprehensive analysis of (prote)omics data', *Nature Methods 2016 13:9*, 13(9), pp. 731–740. doi: 10.1038/nmeth.3901.

Tyanova, S., Temu, T. and Cox, J. (2016) 'The MaxQuant computational platform for mass spectrometry–based shotgun proteomics', *Nature Protocols*, 11. doi: 10.1038/nprot.2016.136.

Vig, A. *et al.* (2020) 'DYNC2H1 hypomorphic or retina-predominant variants cause nonsyndromic retinal degeneration', *Genetics in Medicine*, 22(12), p. 2041. doi: 10.1038/S41436-020-0915-1.

Xun, C. *et al.* (2018) 'Circulating RBP4 Increase and Its Diagnosis of Chronic Kidney Disease', *Annals of clinical and laboratory science*, 48(2), pp. 205–207. Available at: https://pubmed.ncbi.nlm.nih.gov/29678848/ (Accessed: 20 February 2024).

Zaucke, F. *et al.* (2010) 'Uromodulin is expressed in renal primary cilia and UMOD mutations result in decreased ciliary uromodulin expression', *Human Molecular Genetics*, 19(10), p. 1985. doi: 10.1093/HMG/DDQ077.

Zhang, Q. *et al.* (2012) 'Intrinsic protein-protein interaction-mediated and chaperonin-assisted sequential assembly of stable bardet-biedl syndrome protein complex, the BBSome.', *The Journal of biological chemistry*, 287(24), pp. 20625–35. doi: 10.1074/jbc.M112.341487.

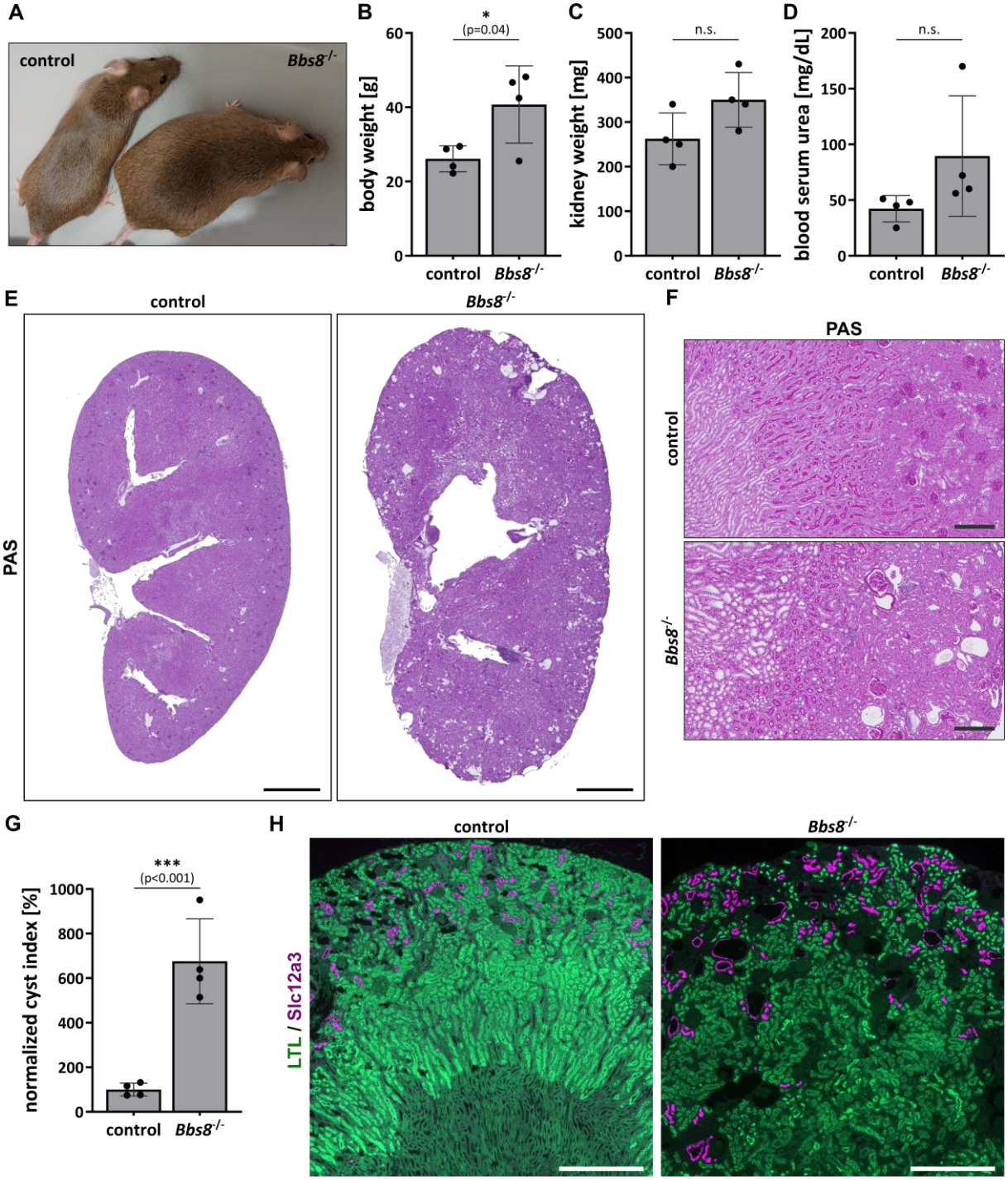
A
control
Bbs8-/-
B
*
(p=0.04)
body weight [g]
60
40
20
0
control
Bbs8-/-
C
n.s.
kidney weight [mg]
500
400
300
200
100
0
control
Bbs8-/-
D
n.s.
blood serum urea [mg/dL]
200
150
100
50
0
control
Bbs8-/-
E
control
Bbs8-/-
PAS
F
PAS
control
Bbs8-/-
G
***
(p<0.001)
normalized cyst index [%]
1000
800
600
400
200
0
control
Bbs8-/-
H
control
Bbs8-/-
LTL / Slc12a3

Figure 1

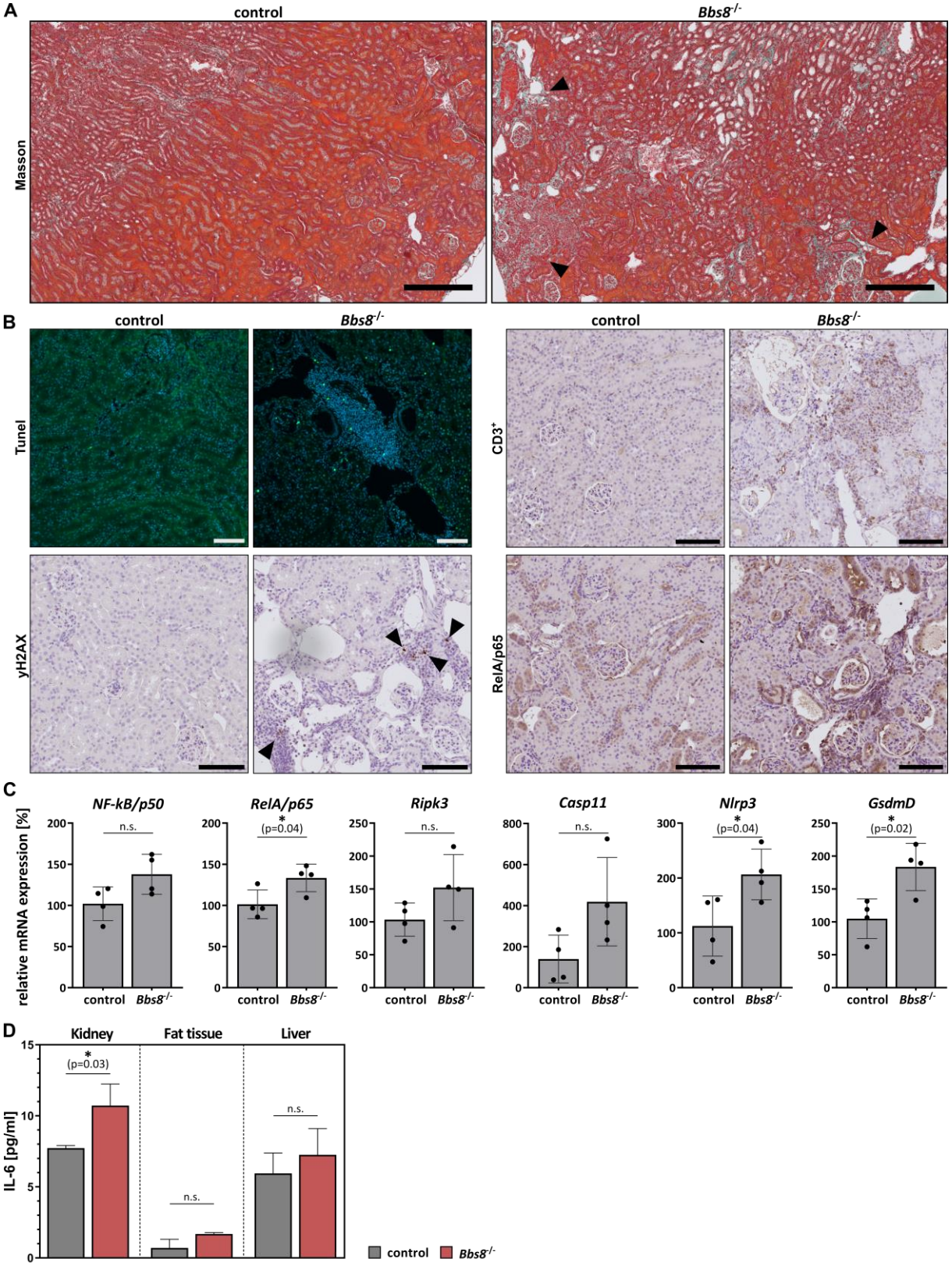
A
control
Bbs8-/-
Masson
B
control
Bbs8-/-
Tunel
control
Bbs8-/-
CD3+
γH2AX
RelA/p65
C
NF-kB/p50
RelA/p65
Ripk3
Casp11
Nlrp3
GsdmD
relative mRNA expression [%]
n.s.
*
(p=0.04)
(p=0.02)
control
Bbs8-/-
D
Kidney
Fat tissue
Liver
IL-6 [pg/ml]
*
(p=0.03)
n.s.
control
Bbs8-/-

Figure 2

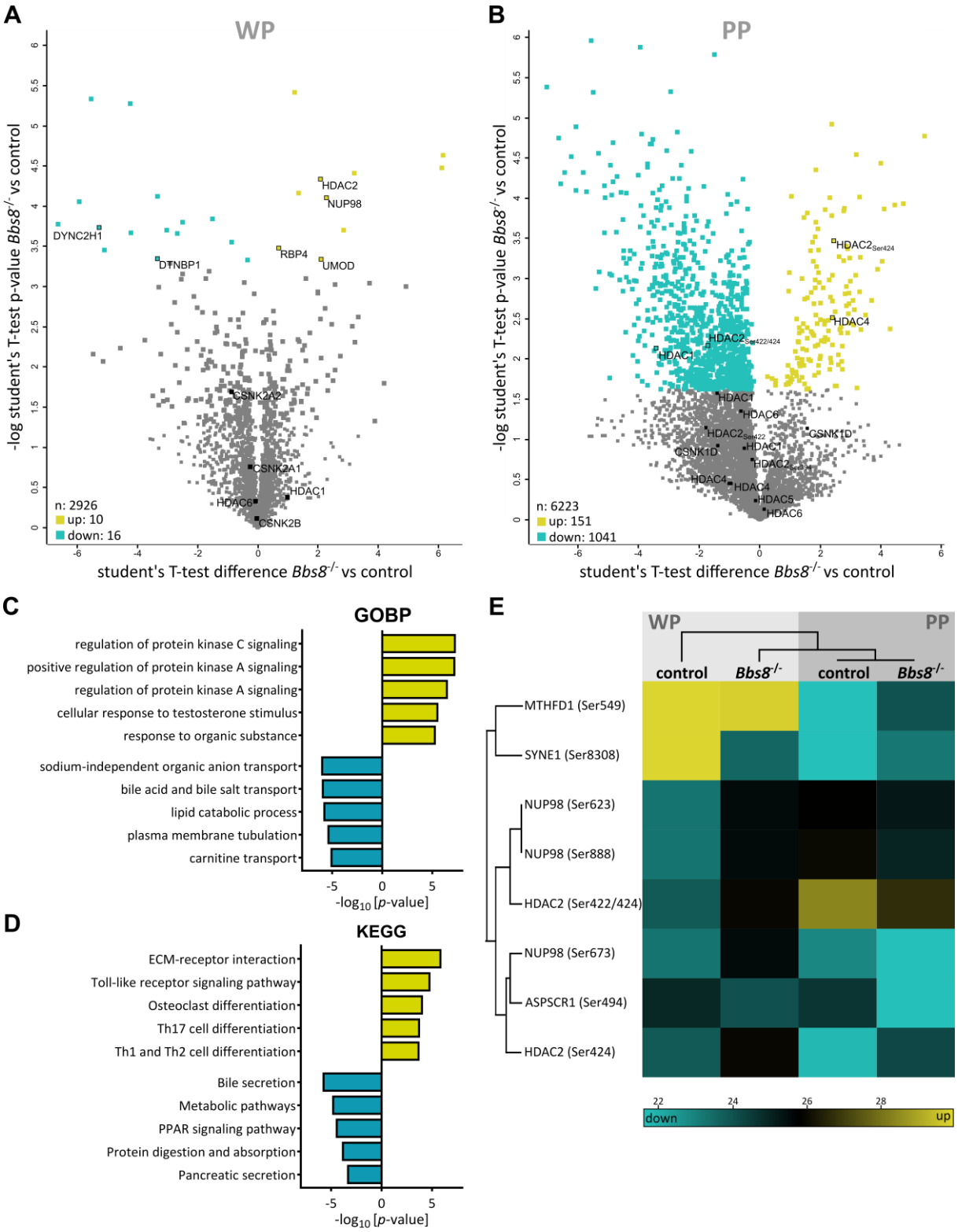
A
WP
-log student's T-test p-value Bbs8-/- vs control
student's T-test difference Bbs8-/- vs control
HDAC2
NUP98
DYNC2H1
RBP4
DTNBP1
UMOD
CSNK2A2
CSNK2A1
HDAC1
HDAC6
CSNK2B
n: 2926
up: 10
down: 16
B
PP
-log student's T-test p-value Bbs8-/- vs control
student's T-test difference Bbs8-/- vs control
HDAC2Ser424
HDAC4
HDAC2Ser422/424
HDAC1
HDAC1
HDAC6
HDAC2Ser422
CSNK1D
CSNK1D
HDAC1
HDAC2Ser424
HDAC4
HDAC4
HDAC5
HDAC6
n: 6223
up: 151
down: 1041
C
GOBP
regulation of protein kinase C signaling
positive regulation of protein kinase A signaling
regulation of protein kinase A signaling
cellular response to testosterone stimulus
response to organic substance
sodium-independent organic anion transport
bile acid and bile salt transport
lipid catabolic process
plasma membrane tubulation
carnitine transport
-log10 [p-value]
D
KEGG
ECM-receptor interaction
Toll-like receptor signaling pathway
Osteoclast differentiation
Th17 cell differentiation
Th1 and Th2 cell differentiation
Bile secretion
Metabolic pathways
PPAR signaling pathway
Protein digestion and absorption
Pancreatic secretion
-log10 [p-value]
E
WP
PP
control
Bbs8-/-
control
Bbs8-/-
MTHFD1 (Ser549)
SYNE1 (Ser8308)
NUP98 (Ser623)
NUP98 (Ser888)
HDAC2 (Ser422/424)
NUP98 (Ser673)
ASPSCR1 (Ser494)
HDAC2 (Ser424)
down
up

Figure 3

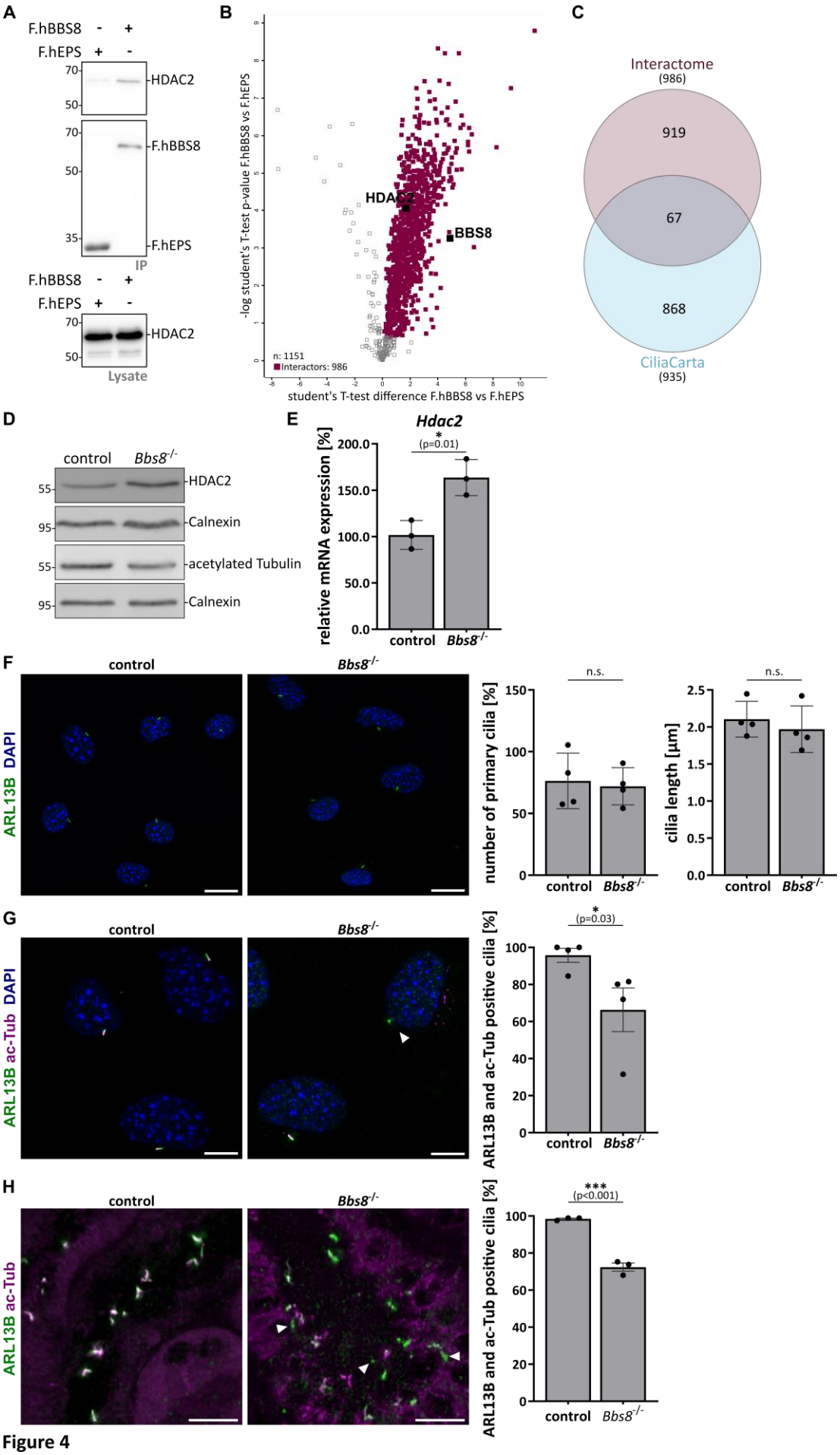
A
F.hBBS8 - +
F.hEPS + -
70
50
HDAC2
70
50
F.hBBS8
35
F.hEPS
IP
F.hBBS8 - +
F.hEPS + -
70
50
HDAC2
Lysate
B
-log student's T-test p-value F.hBBS8 vs F.hEPS
HDAC2
BBS8
n: 1151
Interactors: 986
student's T-test difference F.hBBS8 vs F.hEPS
C
Interactome
(986)
919
67
868
CiliaCarta
(935)
D
control
Bbs8-/-
55
HDAC2
95
Calnexin
55
acetylated Tubulin
95
Calnexin
E
Hdac2
*
(p=0.01)
relative mRNA expression [%]
200.0
150.0
100.0
50.0
0.0
control
Bbs8-/-
F
control
Bbs8-/-
ARL13B DAPI
n.s.
number of primary cilia [%]
150
100
50
0
control
Bbs8-/-
n.s.
cilia length [µm]
2.5
2.0
1.5
1.0
0.5
0.0
control
Bbs8-/-
G
control
Bbs8-/-
ARL13B ac-Tub DAPI
*
(p=0.03)
ARL13B and ac-Tub positive cilia [%]
100
80
60
40
20
0
control
Bbs8-/-
H
control
Bbs8-/-
ARL13B ac-Tub
***
(p<0.001)
ARL13B and ac-Tub positive cilia [%]
100
80
60
40
20
0
control
Bbs8-/-

Figure 4

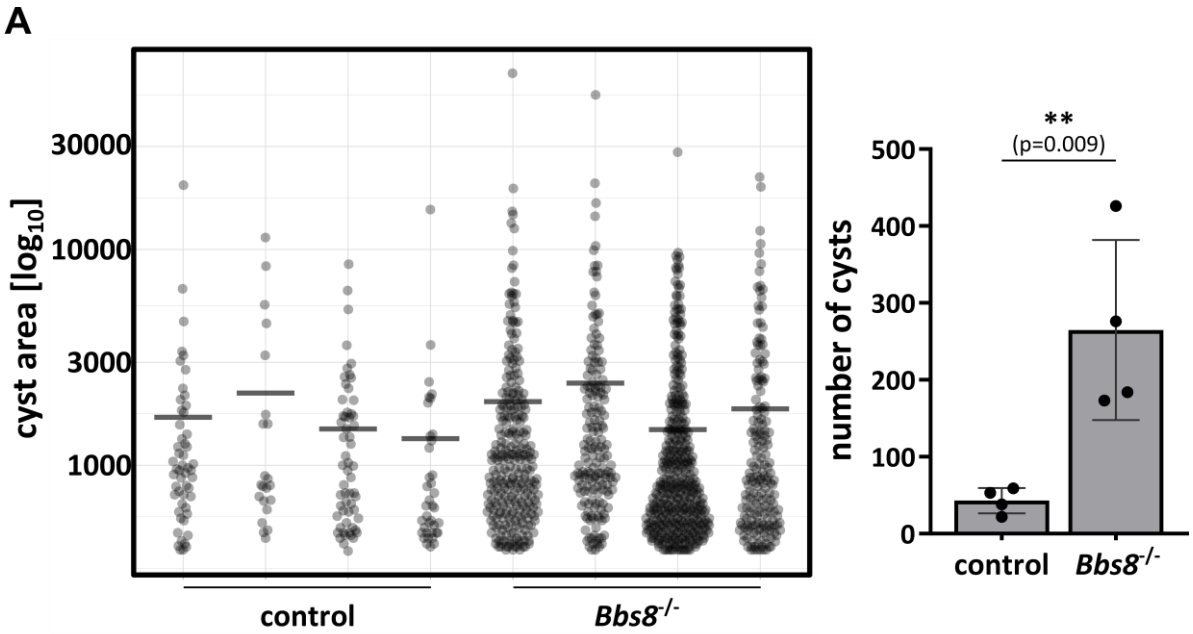

Supplementary figure 1

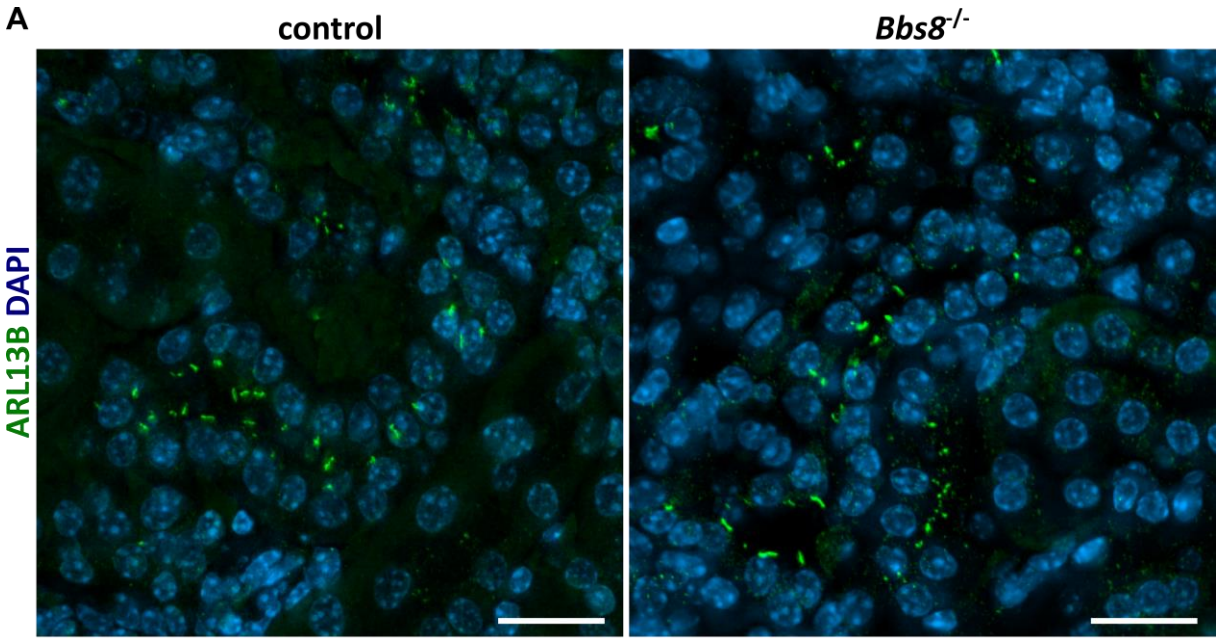

Supplementary figure 2

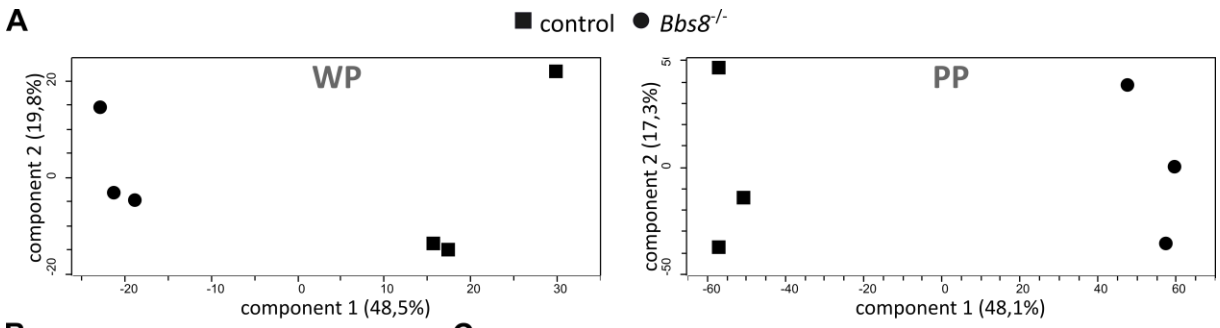

B

Up-Rregulated (-log p-value)		Down-Regulated (-log p-value)	
DCTN6	(5.41)	RBM22	(5.33)
THOC7	(4.63)	APOC1	(5.28)
AGO2	(4.47)	LYRM5	(4.92)
TTN	(4.41)	ACNAT2	(4.13)
HDAC2	(4.33)	GAR1	(4.05)
PARP3	(4.16)	ARHGAP18	(3.84)
NUP98	(4.10)	MRPL47	(3.80)
COPZ2	(3.70)	SYNE1	(3.77)
RBP4	(3.47)	DYNC2H1	(3.73)
UMOD	(3.33)	DAP	(3.70)
		UBE2V2	(3.67)
		NAA15	(3.66)
		ASPSCR1	(3.55)
		SUMO2	(3.46)
		DTNBP1	(3.35)
		MTHFD1	(3.33)

C

Residue	Sig. regulated	Phosphosite
HDAC2 Ser394	-	MLPHAPGVQMQAIPEDAVHEDSGDEDGEDPDKR
HDAC2 Ser422	-	RIACDEEFSDSEDEGEGGRR
HDAC2 Ser424	up	RIACDEEFSDSEDEGEGGRR
HDAC2 Ser422/Ser424	down	RIACDEEFSDSEDEGEGGRR

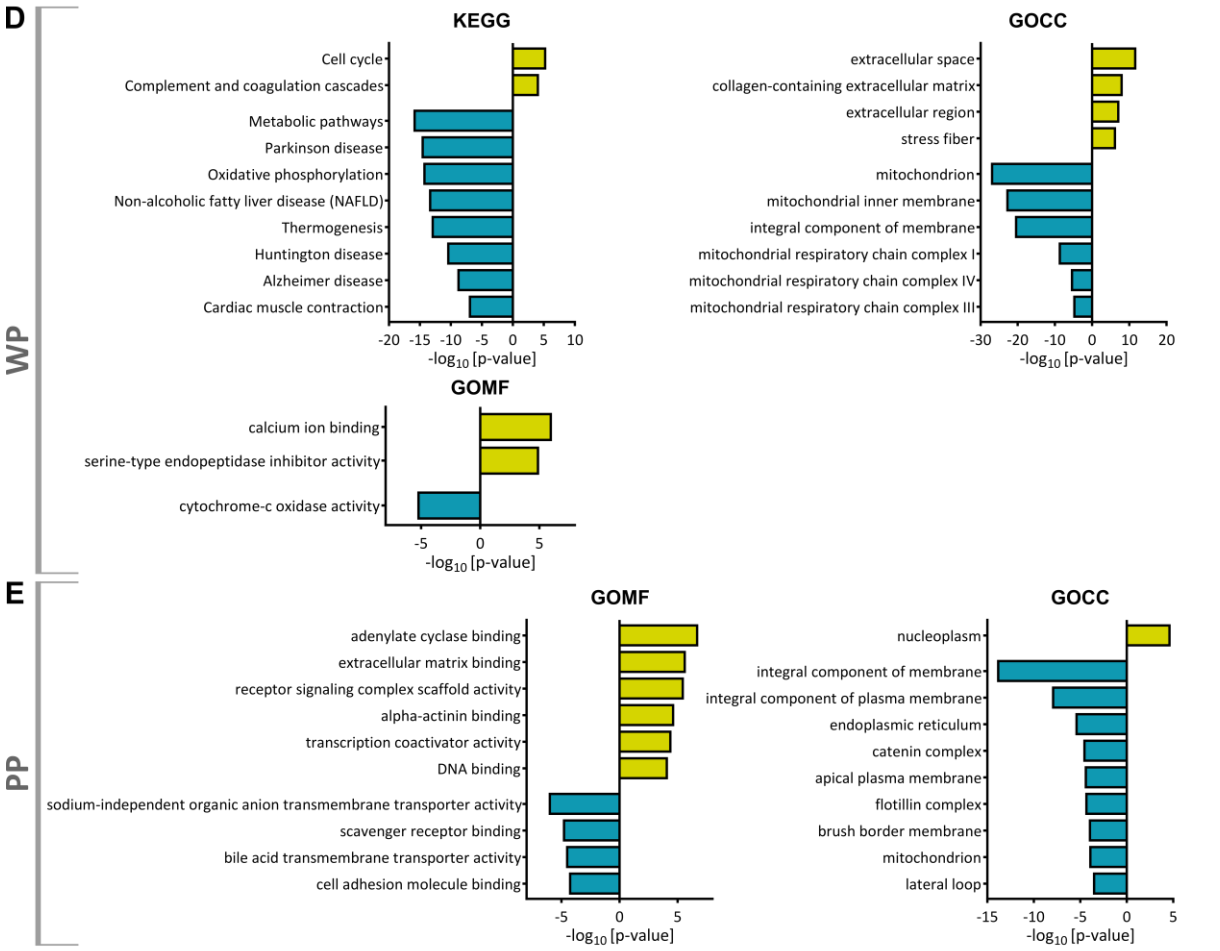

Supplementary figure 3

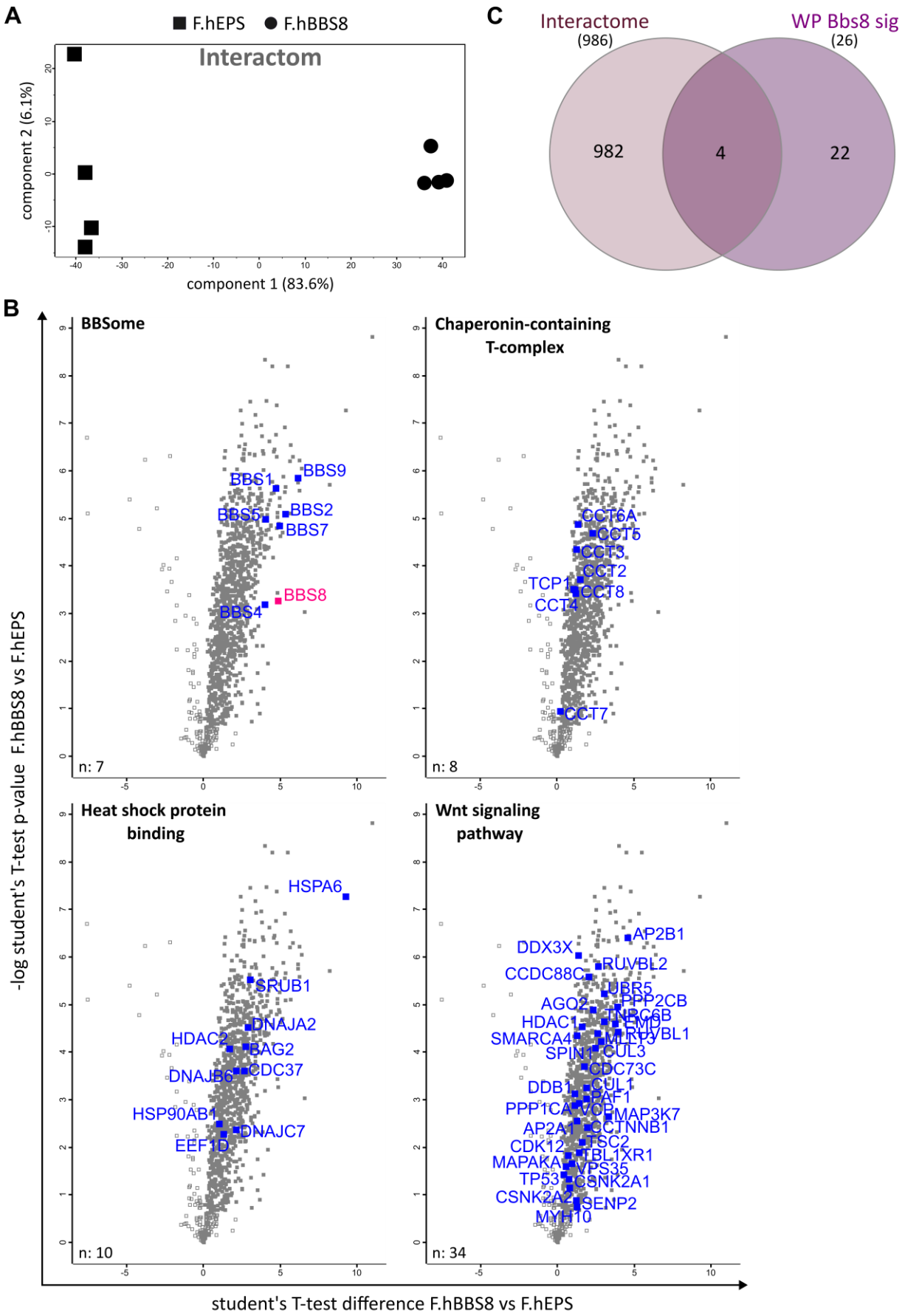

Supplementary figure 4

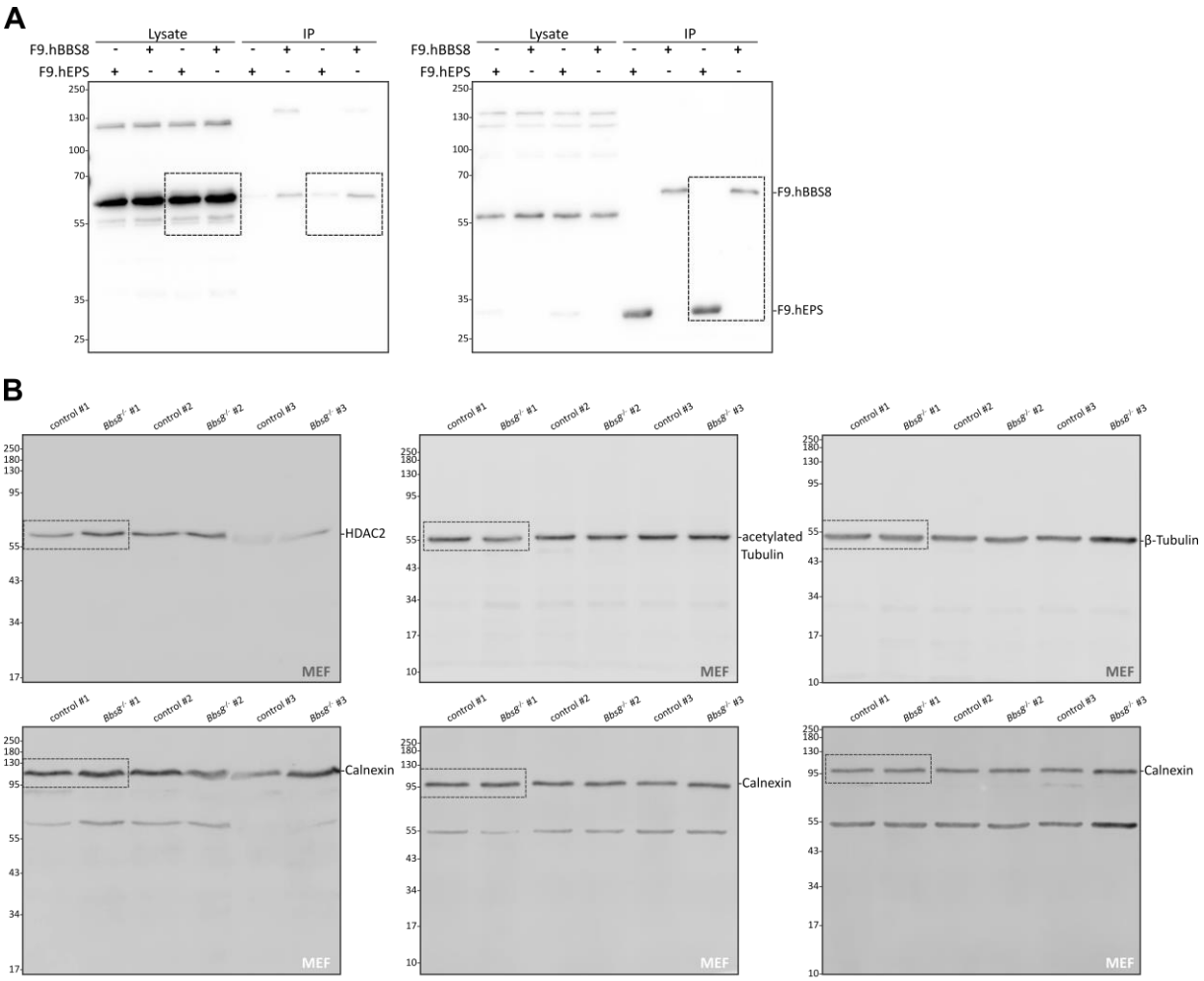

Supplementary figure 5